CWRF downscaling with improved land surface initialization enhances spring-summer seasonal climate prediction skill in China

Han Zhang[a], Xin-Zhong Liang[b,c,*], Yongjiu Dai[a,*], Lianchun Song[d], Qingquan Li[d], Fang Wang[e], Shulei Zhang[a]

[a]*Southern Marine Science and Engineering Guangdong Laboratory (Zhuhai), School of Atmospheric Science, Sun Yat-sen University, Zhuhai, China*

[b]*Department of Atmospheric & Oceanic Science, University of Maryland, Maryland, USA*

[c]*Earth System Science Interdisciplinary Center, University of Maryland, Maryland, USA*

[d]*National Climate Center, China Meteorological Administration, Beijing, China*

**Corresponding authors*: Xin-Zhong Liang, xliang@umd.edu

Yongjiu Dai, daiyj6@mail.sysu.edu.cn

Early Online Release: This preliminary version has been accepted for publication in *Journal of Climate*, may be fully cited, and has been assigned DOI 10.1175/JCLI-D-23-0565.1. The final typeset copyedited article will replace the EOR at the above DOI when it is published.

ABSTRACT

This study investigates skill enhancement in operational seasonal forecasts of Beijing Climate Center's Climate System Model through regional Climate-Weather Research and Forecasting (CWRF) downscaling and improved land initialization in China. The downscaling mitigates regional climate biases, enhancing precipitation pattern correlations by 0.29 in spring and 0.21 in summer. It also strengthens predictive capabilities for interannual anomalies, expanding skillful temperature forecast areas by 6% in spring and 12% in summer. Remarkably, during seven of ten years with relative high predictability, the downscaling increases average seasonal precipitation anomaly correlations by 0.22 and 0.25. Additionally, substitution of initial land conditions via a Common Land Model integration reduces snow cover and cold biases across the Tibetan Plateau and Mongolia-Northeast China, consistently contributing to CWRF's overall enhanced forecasting capabilities.

Improved downscaling predictive skill is attributed to CWRF's enhanced physics representation, accurately capturing intricate regional interactions and associated teleconnections across China, especially linked to the Tibetan Plateau's blocking and thermal effects. In summer, CWRF predicts an intensified South Asian High alongside a strengthened East Asian Jet compared to CSM, amplifying cold air advection and warm moisture transport over central to northeast regions. Consequently, rainfall distributions and interannual anomalies over these areas experience substantial improvements. Similar enhanced circulation processes elucidate skill improvement from land initialization, where accurate specification of initial snow cover and soil temperature within sensitive regions persists in influencing local and remote circulations extending beyond two seasons. Our findings emphasize the potential of improving physics representation and surface initialization to markedly enhance regional climate predictions.

Accepted for publication in *Journal of Climate*. DOI 10.1175/JCLI-D-23-0565.1.

1. Introduction

Regional climate models (RCMs) are widely recognized for added value to their driving general circulation models (GCMs) from more realistic physics representation at higher resolution (Roads et al. 2003; Liang et al. 2004a,b, 2006, 2019; Diffenbaugh et al. 2005; Prein et al. 2015; Rummukainen 2016; Giorgi 2019). RCM downscaling has demonstrated skill enhancement for seasonal predictions in North America (Cocke et al. 2007; Lim et al. 2007; Yuan and Liang 2011a; Liu et al. 2016), South America (De Sales and Xue 2006), Europe (Diez et al. 2011; Patarčić and Branković 2012; Sangelantoni et al. 2019), and Asia (Sun et al. 2006; Ding et al. 2006a,b; Yuan et al. 2012; Van et al. 2014; Ma et al. 2015). Enhanced skill for surface air temperature and precipitation was often attributed to RCMs' better representation of orographic effects with higher resolution. However, RCM downscaling performance is highly sensitive to physics parameterization schemes, highlighting the critical importance of consistent representation of cumulus, microphysics, radiation, planetary boundary layer, and surface processes as well as their interactions (Liang et al. 2004b, 2007; Yuan et al. 2012; Sun and Liang 2020a,b; Zhang et al. 2023).

China features complex topography and spans multiple climate zones with distinct physical processes. In summer, prevailing large-scale circulations include the East Asian Jet (EAJ), the South Asian High (SAH), the Western Pacific Subtropical High (WPSH), and the Intertropical Convergence Zone (Liang et al. 1995; Lau and Yang 1996; Liang and Wang 1998; Samel et al. 1999; Yang et al. 2004; Wang et al. 2011) along with mesoscale features such as low-level jets and vortices (Wang 1987; Ding and Chan 2005; Luo et al. 2013). They collectively shape China's climate characteristics, making seasonal predictions, particularly for interannual anomalies, more challenging (Wang et al. 2015, 2022; Ren et al. 2019). However, the combined influences of planetary and regional processes render RCMs more effective for application in China. Liang et al. (2019) demonstrated that the Climate extension of the Weather Research and Forecasting model (CWRF, Liang et al. 2012) outperforms its driving global reanalysis and a popular RCM in reproducing China climate characteristics, including monsoon rain bands, diurnal temperature ranges, surface winds, interannual precipitation and temperature anomalies, and extreme precipitation. The CWRF has recently been adopted by Beijing Climate Center (BCC, designated by the World Meteorological Organization as the Regional Climate Centre for Asia) to make operational seasonal forecasts. Its initial testing operation for the last three years has shown persistent performance

Accepted for publication in *Journal of Climate*. DOI 10.1175/JCLI-D-23-0565.1.

in summer precipitation prediction superior to other existing dynamical and statistical products. While Zhang et al. (2023) provided a preliminary evaluation of the CWRF skill enhancement over the BCC Climate System Model (BCC_CSM) for China summer precipitation hindcasts during 1991-2010, this study offers a more systematic assessment and process understanding of its performance for spring-summer forecasts in the operational framework and examine the sensitivity to land surface initialization.

Global oceans and land are identified as two major sources of seasonal predictability. As GCMs integrate and transfer oceanic forcing (or predictive) signals into planetary circulations that form the lateral boundary conditions driving RCMs, the downscaling incorporates the predictability from the land source (surface and deep soil) that occurs as initial anomalies within the computational domain and coupled land-atmosphere memory evolving during the prediction. Koster et al. (2004) and Notaro (2008) discovered that strong land-atmosphere coupling in certain regions over North America enables deep soil predictability for local summer surface temperature up to two months in advance. Prodhomme et al. (2016) reported that using accurate land-surface initial conditions improves seasonal predictions in Europe. Orsolini et al. (2013), and Thomas et al. (2016) showed that a more realistic initialization of snow cover enhances sub-seasonal to the seasonal climate predictive skill through feedback mechanisms. Snow cover in Eurasia and high mountains can produce lagged remote influences on precipitation in China (Liang et al. 1995; Zuo et al. 2011; Wang et al. 2017; Broxton et al. 2017). Most recently, Xue et al. (2021) proposed the Impact of Initialized Land Surface Temperature and Snowpack on Subseasonal to Seasonal Prediction Project (LS4P) to focus on the remote effects of initial land surface temperature and subsurface conditions over high mountains. Xu et al. (2022) revealed that early spring deep soil temperature in the Tibetan Plateau acts as a charged capacitor, modulating the SAH and EAJ, leading to significant spring-summer precipitation anomalies in eastern China. Xue et al. (2022, 2023) highlighted that high-mountain land temperature could produce 40% of observed anomalies for sub-seasonal to seasonal precipitation, a contribution comparable to that of sea surface temperature.

However, few RCM studies have examined the downscaling skill enhancement and sensitivity to land surface initialization on seasonal climate prediction within the actual operational forecast framework. The present study addresses this topic based on the CWRF downscaling seasonal predictions over China from the global BCC_CSM operational

Accepted for publication in *Journal of Climate*. DOI 10.1175/JCLI-D-23-0565.1.

forecasts in the China Meteorological Administration. Section 2 presents the model description, observational data, and experiment design. Section 3 evaluates the results, including the skill enhancement from the CWRF downscaling and land initialization on seasonal mean climate and interannual variation for regional temperature and precipitation in China. Section 4 discusses the key physical processes and underlying mechanisms that are responsible for the prediction improvements. Section 5 gives the conclusion.

2. Model, Data, and Experiment Design

A two-tier-nested method is used for making seasonal climate predictions. The first tier uses a coupled GCM to make the first-guess forecast of global circulation conditions. The second tier uses an RCM to downscale the global forecast into regional climate prediction in China with higher resolution. In the control prediction, the RCM takes initial atmospheric and land conditions as well as time-varying lateral boundary and sea surface conditions directly from the GCM's output. An experimental prediction is also made to substitute the initial land conditions with the output from a standalone land model integration driven by a reanalysis.

a. Model Description

The GCM used is the BCC_CSM version 1.1m (hereafter referred to as CSM), which fully couples atmosphere, land, ocean, and sea ice components (Wu et al. 2014). The atmosphere component (AGCM2.2) uses a horizontal grid of T106 (triangular truncation at grid spacing about 110 km) and 40 layers of hybrid sigma pressure, with the top to 0.5 hPa. The land component (AVIM1.0) shares the same T106 horizontal resolution as the atmosphere (Ji et al. 2008). The ocean component (MOM4) uses a tripolar grid with variable horizontal grids of 1/3°-1° and 40 vertical layers (Griffies et al. 2005). The sea ice component (SIS) shares the same ocean horizontal grid with 3 vertical layers (Winton 2000).

The RCM used is the CWRF (Liang et al. 2012), which has been continuously developed and systematically evaluated for regional climate downscaling and applications in the United States, including seasonal climate prediction (Yuan and Liang 2011a; Chen et al. 2016; Liu et al. 2016), and most recently, extreme precipitation improvement (Sun and Liang 2020a,b), longstanding bias correction (Sun and Liang 2022, 2023), and agricultural decision support (Liang et al. 2024). The CWRF has also been rigorously evaluated in China with superior performance (Liang et al. 2019). It has been increasingly used in China for sensitivity analysis, process understanding, present climate simulation (Wei et al. 2021; Li et al. 2021;

Accepted for publication in *Journal of Climate*. DOI 10.1175/JCLI-D-23-0565.1.

Shi et al. 2021; Xu et al. 2022; Zhang et al. 2023; Zhao and Liang 2024; Zhao et al. 2024), and future projection (Liu et al. 2013; Jiang et al. 2021). In 2018, BCC adopted CWRF as the core of the regional prediction system and has since been making operational seasonal forecasts with a promising skill for summer precipitation outlook in China.

The CWRF physics configuration used is identical to that designed by Liang et al. (2019), which includes the Ensemble Cumulus Parameterization (ECP, Qiao and Liang 2015, 2016, 2017), the GSFCGCE Microphysics (Tao et al. 2003), the XRL diagnostic Cloud (Xu and Randall 1996; Liang et al. 2004), the prescribed MISR Aerosol (Kahn 2005; Kahn et al. 2007; Zhao et al. 2009), the GSFCLXZ Radiation (Chou and Suarez 1999; Chou et al. 2001) as coupled in the Cloud-Aerosol-Radiation ensemble model (Zhang et al. 2013a,b), the improved CAM plus ORO Planetary Boundary Layer parameterization (Holtslag and Boville 1993; Rontu 2006; Liang et al. 2006b), and the Conjunctive Surface-Subsurface Process (CSSP, see below for details). Since RCM downscaling performance is sensitive to the domain configuration (Liang et al. 2001; Xue et al. 2014), we adopt the same domain (Figure S1) as tested by Liu et al. (2008) and well evaluated by Liang et al. (2019). The domain uses a Lambert conformal projection with a center at 35.18°N and 110°E and a grid spacing of 30km, totaling 272 EW×172 SN grids. The model has 36 terrain-following sigma levels with the top at 50 hPa.

The CSSP is originated from the early version of the Common Land Model (CoLM, (Dai et al. 2003, 2004) with significant improvements. The major CSSP advances from CoLM include surface-subsurface flow interaction (Choi et al. 2007, 2013; Choi and Liang 2010; Yuan and Liang 2011b), representation of subgrid topographic control on soil moisture, and, most relevant to this study, an improved land surface albedo parameterization (Liang et al. 2005). Rooted in the Biosphere-Atmosphere Transfer Scheme (BATS, Dickinson et al. 1993), the albedo scheme consists of three components: bare soil, vegetation, and snow. The soil albedo depends on static soil properties (sand, clay, organic content) and time-varying soil moisture, while the vegetation albedo is a function of leaf and stem area indices and dominant vegetation type. When snow is absent, the albedo is a linear combination of the soil and vegetation albedos as weighted by the vegetation cover fraction. When snow is present, its albedo depends on snow age and zenith angle and the total albedo is determined as a linear combination of the three component albedos as weighted by the snow and vegetation cover fractions. This albedo parameterization enables CSSP to characterize the local thermal-water

Accepted for publication in *Journal of Climate*. DOI 10.1175/JCLI-D-23-0565.1.

feedback process combined with the snowmelt infiltration process and soil-vegetation evapotranspiration process (Liang et al. 2005). Besides these advances, CSSP shares many features with CoLM, including the internal initialization method and vertical structure, resulting in a comparable performance of soil temperature and moisture prediction. The similarity between CSSP and CoLM for model setup and performance is the reason we choose CoLM to provide the standalone reanalysis-driven land initialization.

The CoLM combines the advantages of the Land Surface Model (Bonan 1996), the Biosphere-Atmosphere Transfer Scheme (Dickinson et al. 1993), and the Institute of Atmospheric Physics, Chinese Academy of Sciences Land Surface Model (Dai and Zeng 1997; Dai et al. 1998). It incorporates key land surface processes such as a two-big-leaf model (Wang and Leuning 1998), a two-stream approximation for radiative transfer (Coakley and Chylek 1975), and a topography-based runoff parameterization (Beven and Kirkby 1979; Ambroise et al. 1996). The CoLM integrates interactions among the atmospheric boundary, vegetation canopy, snow cover, and soil processes. Extensive standalone and coupled model studies have demonstrated that the CoLM can reasonably estimate land surface energy fluxes and characteristics (Dai et al. 2003; Li et al. 2012, 2017; Xin et al. 2019). This study uses the CoLM version 2014 at a globally uniform 0.5° grid spacing.

b. Experiment Design

Table 1 lists the three forecast experiments compared in this study. All forecasts are initialized each year on March 2 and end on August 31 from 1991 to 2014, encompassing two seasons. The respective workflow of these forecasts is as follows:

1. The CSM forecasts begin on February 1 with fast nudging toward the NCEP-NCAR-R1 reanalysis (Kistler et al. 2001) continuously till March 1 and are then integrated forward freely. The nudging applies to only atmospheric circulation variables, including winds, geopotential height, air temperature, and vapor mixing ratio. The land component has no nudging treatment but uses the climatology as the initial condition. It is acknowledged that, NCEP-NCAR-R1 is not as advanced as newer reanalysis datasets such as the NCEP/DOE R2 (Kanamitsu et al. 2002), the NASA MERRA-2 (Gelaro et al. 2017), or the ECMWF ERA5 (Hersbach et al. 2020). However, it has a faster timeline of data availability (2 days behind real time) than those latest reanalysis datasets, and therefore was chosen by China Meteorology Administration as the initial nudging dataset for the CSM operational forecast.

Accepted for publication in *Journal of Climate*. DOI 10.1175/JCLI-D-23-0565.1.

As an extension of the present operational practice, this study follows the same procedure in all experiments.

2. The CWRF control (CTL) forecast begins on March 2 with initial conditions of both the atmosphere and land directly from the corresponding CSM forecast and integrates forward with time-varying 6-hourly lateral boundary conditions from the same CSM forecast.

3. The CWRF experiment (EXP) forecast is identical to the CTL forecast except that initial land conditions are substituted from a standalone CoLM continuous integration driven by an observation-reanalysis fused dataset CRUNCEP (Viovy 2018) from January 1, 1975, to December 31, 2014. Taking from this CoLM integration after a well spin-up for 16 years, the initial land conditions, including surface and soil temperatures, soil liquid and ice water contents, and snow water equivalent (SWE), on March 2 of each year between 1991-2014 have reached a quasi-equilibrium with the observed atmospheric forcing.

4. The IST and ISN experiments are identical to CTL except that the initial soil temperature and SWE states were replaced from EXP for IST and ISN respectively. In CoLM and CSSP, snow cover fraction (SCF) is diagnosed following Niu and Yang (2007):

$$\mathrm{SCF} = tanh\left(\frac{\mathrm{SNP}}{2.5z_{0g}\left(\frac{\mathrm{SWE}}{\mathrm{SNP}\cdot\rho_{\mathrm{new}}}\right)^{\alpha}}\right) \qquad \text{Eq (1)}$$

where SNP is snow depth [m], SWE is snow water equivalent [m], $\rho_{\mathrm{new}} = 100$ is fresh snow density [kg m^{-3}], $z_{0g} = 0.01$ is ground roughness [m], and $\alpha = 1$ is a melting factor. While SWE is predicted as the balance of snowfall, interception, and melt rates, SNP is initialized from SWE dividing by snow density (250 kg m^{-3}) and integrated forward with snow accumulating, compacting, and melting processes. Thus, the substitution of SWE changes entirely the initial snow states, including both SCF and SNP.

Forecast name	**Initialization**	**Forecast period**	**Goal**
CSM	Nudged to the NCEP-NCAR-R1 reanalysis atmospheric conditions during	Each year initialized on March 2 and end on August 31 during 1991-2014	Make global circulation forecasts to provide driving conditions for CWRF

Accepted for publication in *Journal of Climate*. DOI 10.1175/JCLI-D-23-0565.1.

	February 1 to March 1		
CTL	Both atmospheric and land initial conditions are directly from CSM		Make CWRF downscaling prediction driven by CSM
EXP	Initial atmospheric conditions are from CSM, while land conditions are from the standalone CoLM integration driven by CRUNCEP		Determine the effect of land initialization on CWRF prediction performance
IST	Initial conditions are kept same with CTL, while soil temperature is same as EXP		Identify the influence of initial soil temperature
ISN	Initial conditions are kept same with CTL, while SWE is same as EXP		Identify the influence of initial snow states

Table 1. Experiment design.

c. Observational Data

The NCEP-NCAR-R1 reanalysis (Kistler et al. 2001) is used to nudge atmospheric circulation conditions as observed in the prior month (February) to obtain the initial states on March 2 for the CSM forecasts. The CRUNCEP v7.0 (Viovy 2018) 6-hourly forcing data, which combines the CRU TS3.2 observations and NCEP-NCAR-R1 reanalysis (Harris et al. 2014), is used to drive the standalone CoLM integration that provides initial land states for the CWRF EXP forecasts.

Accepted for publication in *Journal of Climate*. DOI 10.1175/JCLI-D-23-0565.1.

For model evaluation, daily data of surface air temperature at 2m (T2M) and precipitation (PR) are from the CN05.1 (Wu and Gao 2013). The CN05.1 dataset is an observational analysis at a grid spacing of 0.25° in China based on measurements at 2416 standard ground stations. The provider uses the thin-plate spline method and angular distance weight method to interpolate quality-controlled measurement data to a uniformed 0.25° grid. The CN05.1 is not only widely used in regional climate modeling research (Liang et al. 2019; Jiang et al. 2023, Gu et al. 2023; Zhao and Liang 2024), but also adopted by China Meteorological Administration as the reference data to verify and evaluate its operational forecasts. This study uses CN05.1 over mainland China with a supplement outside by the Asian Precipitation-Highly-Resolved Observational Data Integration Towards Evaluation (APHRODITE, Yatagai et al. 2007). Monthly mean land surface temperature (LST) is from the All-weather MicroWave Land Surface Temperature (MW-LST) global data (Fennig et al. 2017) at a grid spacing of 0.25°. Monthly mean SCF is from the MODIS products MOD10CM at a grid spacing of 0.05° (Hall and Riggs 2021). All observational data are bilinearly mapped onto the CWRF grid for subsequent model evaluations.

3. Results

a. Initialization Effects on the Land State of the Initial Month

By design EXP differs from CTL only in initialization, specifying initial land conditions from the observation-driven CoLM integration rather than directly from the CSM output. In both cases, initialization brings initial shocks due to formulation differences among the land components CSSP, CoLM, and AVIM1.0. In addition, observational land/soil data are limited or contain large uncertainty. In particular, satellite products have many missing or poor-quality data on a daily basis due to cloud contamination, while the other assimilation or reanalysis datasets are still model products using land components different from CSSP or CoLM. Therefore, it is more appropriate to evaluate the initialization effects on the initial land state by comparing the average conditions of the first month (March) rather than the instant values on the first day of the forecast. Due to the lack of credible SWE observations and the more direct SCF effect on surface radiation, we use SCF rather than SWE as a proxy for snow states in the subsequent model evaluation or experiment comparison.

Figure 1 compares CTL and EXP predicted March mean biases in SCF, LST, and surface air temperature at 2m (T2M). Two major biases over broad regions are identified with land

Accepted for publication in *Journal of Climate*. DOI 10.1175/JCLI-D-23-0565.1.

surface conditions. First, on the Tibetan Plateau, CTL substantially overestimates SCF in most areas by 30.3% on average, while EXP essentially eliminates the overestimation in the eastern areas, shrinking the regional average bias to 21.5%. More snow cover causes colder LST biases in the corresponding areas, and EXP reduces the CTL biases from -6.7 to -4.2 ºC as averaged on the Tibetan Plateau; the respective T2M biases are reduced from -6.8 to -5.4 ºC. Note that the CN05.1 data for T2M contain substantial uncertainty on the Tibetan Plateau with rare ground observations (Wu and Gao 2013). Basically, there is no ground truth to define actual model "biases". We keep using this phrase subsequently just for simplicity with large uncertainty implied over the Plateau. Nonetheless, it is important to see that the difference between EXP and CTL is 1.4 ºC on average over the entire Tibetan Plateau, which is statistically significant at the 5% significance level and consistent with the snow removal. Second, over large areas across Mongolia and Northeast China, CTL broadly overestimates SCF by 19.9% on average and hence produces colder LST and T2M biases by -2.8 ºC. These CTL regional biases are mostly corrected in EXP. Overall, EXP shows systematic improvements over CTL for snow cover and surface temperatures. However, EXP tends to produce warmer LST than CTL by 2 ºC across southeastern to northern China, whereas both EXP and CTL predict colder LST than the satellite product MW-LST by 2-4 ºC in the desert regions across Xinjiang to western Inner and southern Mongolia, and reversely by 4-8 ºC warmer in the wet monsoon regions across eastern India to southern Asia. No obvious biases are shown in T2M over these regions. This disconnection between surface skin and air temperatures may indicate LST inconsistency as represented in the model versus MW-LST or uncertainty in satellite retrievals.

Accepted for publication in *Journal of Climate*. DOI 10.1175/JCLI-D-23-0565.1.

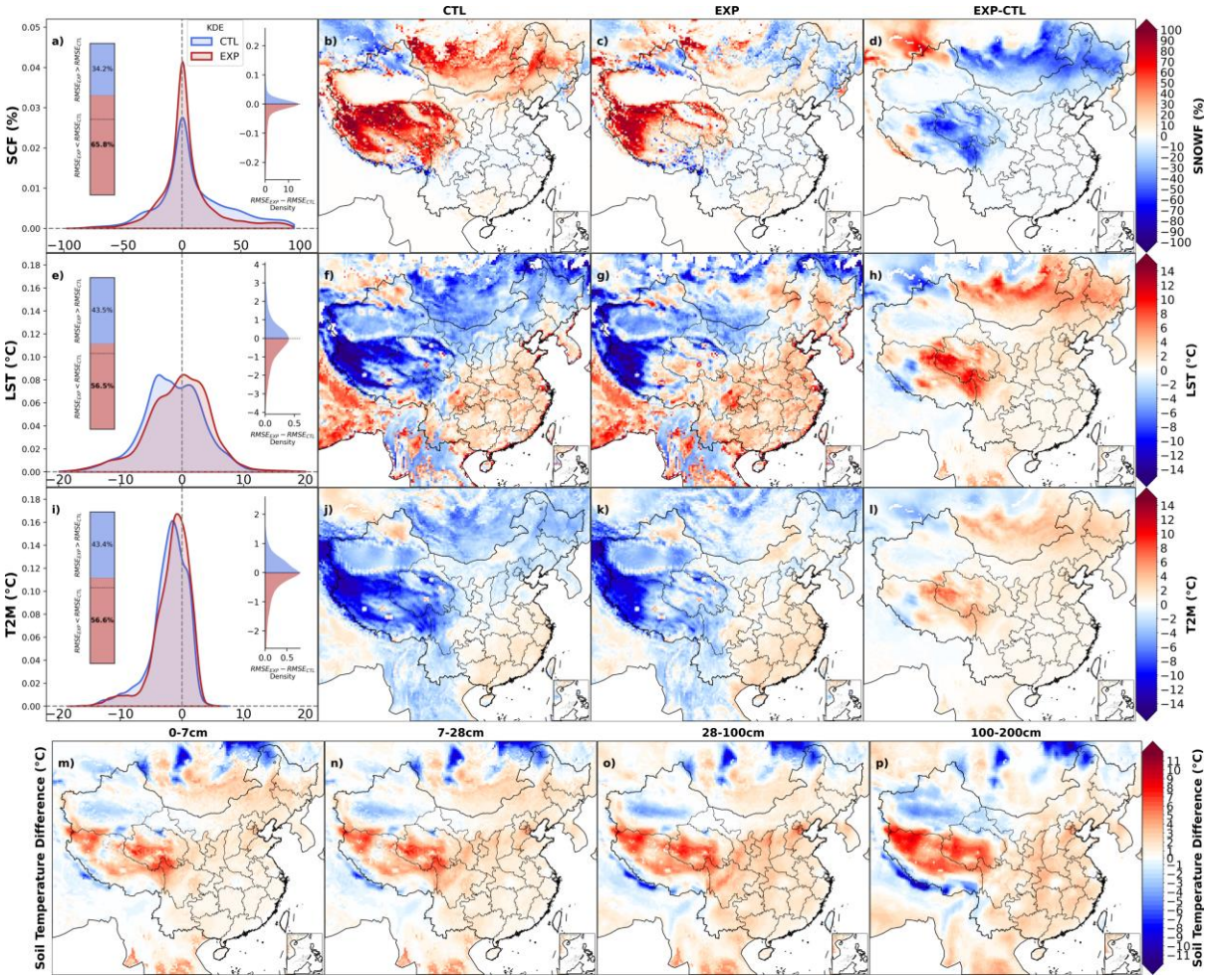

Figure 1. The kernel density and geographic distribution of long-term mean biases of SCF [%] (**a-d**), LST [°C] (**e-h**), and surface air temperature at 2-meter (T2M [°C], **i-l**) in March predicted by CTL and EXP and their differences (EXP minus CTL) as well as soil temperature differences [°C] in four layers (**m-p**). Statistics of SCF and LST are based on 2000-2014 as limited by observational data. In each kernel density plot (**a, e, i**), the left bar chart depicts the proportion of grids having EXP-CTL increased (*blue*) versus decreased (*red*) RMSE while the right inset shows the kernel density of EXP-CTL RMSE differences. For SCF's kernel density estimation, grid points with its climatological mean fraction less than 10% are filtered out to capture key bias statistics. The differences colored on the maps are statistically significant at the 5% significance level with a student's t-test.

Lacking reliable direct observations, Figure 1(m-p) compare EXP minus CTL differences (rather than biases) in soil temperature among 4 layers. In the Tibet Plateau, EXP is warmer than CTL by 4-5°C in the top layer (0-7cm) and 6-8°C covering broader areas in deeper layers. In Mongolia and northern China, EXP is about 2-3°C warmer than CTL in upper layers (0-28cm) and has little difference in deeper layers. In eastern China, EXP is about 2-3°C warmer than CTL in deep layers (28-200cm) but has little difference in upper layers. As discussed below, some soil thermal differences directly resulted from initial shocks may

Accepted for publication in *Journal of Climate*. DOI 10.1175/JCLI-D-23-0565.1.

dissipate shortly, while others can have persistent impacts on land-atmosphere interaction beyond a few months.

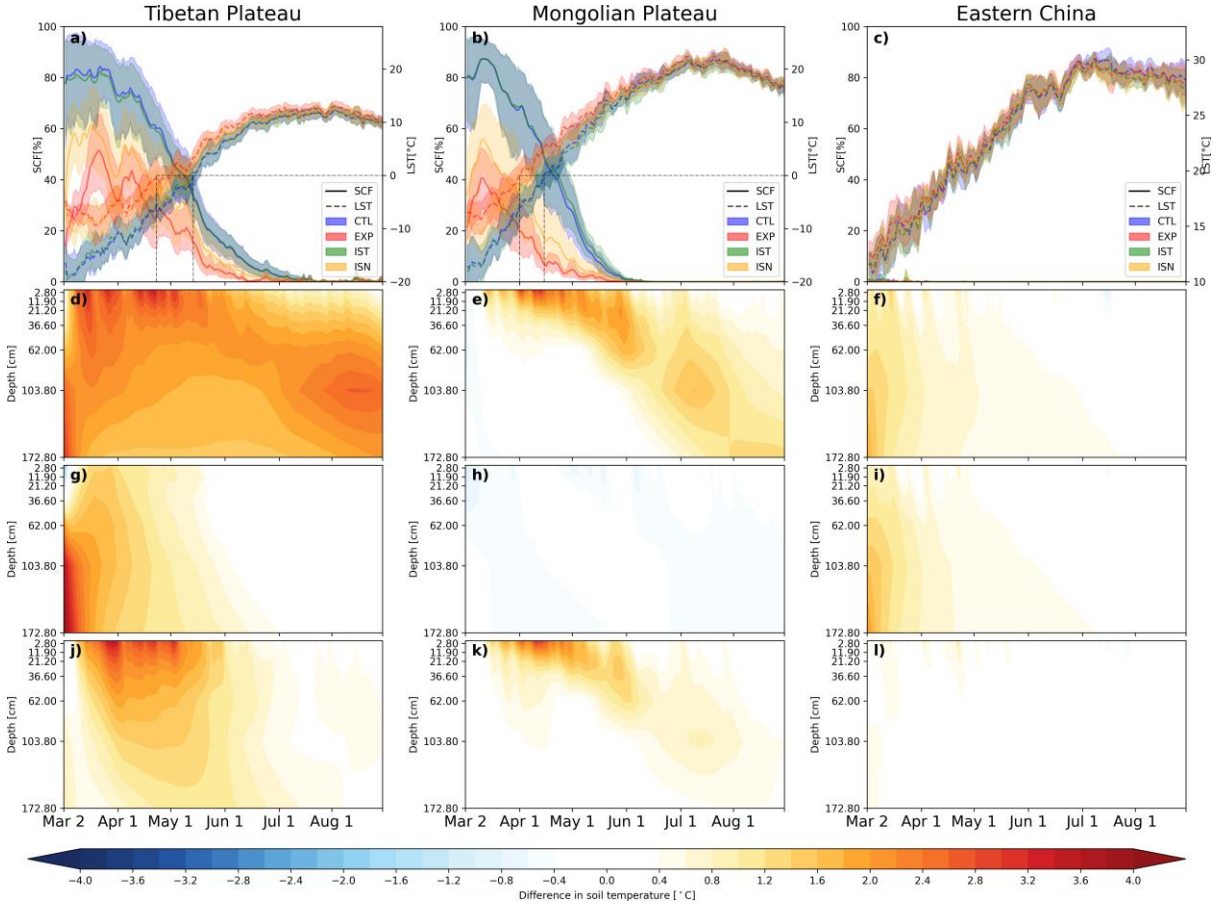

Figure 2. The time evolution during the entire forecast period of daily mean SCF [%] and LST [°C] from CTL, EXP, IST, and ISN (**a-c**) as well as differences in soil temperature [°C] (**d-f:** EXP-CTL, **g-i**: IST-CTL, **j-l**: ISN-CTL) averaged in the Tibetan Plateau (**a, d, g, j**), the Mongolian Plateau (**b, e, h, k**), and eastern China (**c, f, i, l**) between 1991-2014. The color shaded area in (**a-c**) indicates the 99% confidence interval.

As shown in Figure 1, SCF noticeably differs between EXP and CTL on the Tibetan and Mongolian Plateaus. To investigate how such initial perturbations evolve with local and remote impacts, Figure 2 compares daily mean variations of regional average SCF, LST, and soil temperature profiles during the entire forecast period. Regional means are calculated separately on the two Plateaus over all grids with initial SCF differences larger than 25%. The variations in eastern China, averaged over all grids regardless of SCF, are also compared to demonstrate how the result differences over remote areas with no significant differences in initial conditions. On the Tibetan Plateau, EXP shows persistently lower SCF and warmer LST than CTL until early June, while its warmer soil temperature differences from CTL

Accepted for publication in *Journal of Climate*. DOI 10.1175/JCLI-D-23-0565.1.

continue throughout March to August with two distinct features. First, the CoLM initialization has systematically warmer soil in all layers than CSM and the initial perturbations gradually weaken as snow cover keeps decreasing in March and April. Second, the removal of excessive snow cover causes increasingly more solar radiation heating to warm land surface and penetrating deeper soil layers with a clear downward propagating and strengthening signal. A warm core of 3.8°C appears around 1m depth in the mid-August and remains strong into September. Comparing CTL and EXP with IST and ISN clearly shows that the initial snow states pose persistent influences on soil temperature on the Tibetan Plateau. However, only when both initial soil temperature and snow cover states are replaced as in EXP, a noticeable warm center emerges in the deep soil in summer. This implies a nonlinear interaction between deep soil and atmosphere on the Tibetan Plateau.

On the Mongolian Plateau, EXP also has lower SCF and warmer LST than CTL until mid-May, but the differences are much smaller in magnitude and end about a month earlier than those on the Tibetan Plateau. Consistent with ISN and IST, smaller initial snow amounts induce smaller (1-2°C) soil warming perturbations, which are limited only to upper layers (0-30cm) before mid-April; after that, a similar downward propagation of warmer soil perturbations results from the increased solar radiation heating caused by the decreased snow cover. This propagating signal persists into September, albeit much weaker than that on the Tibetan Plateau and negligible in upper layers. In eastern China, given no snow cover change, EXP differs from CTL mainly because of initial warmer soil perturbations, which decay continuously to negligible values before April in upper layers and August in deeper layers; there is no propagating signal as in the two Plateaus. Given that IST shows much smaller changes from CTL, the LST differences between EXP and CTL result mostly from the differences in initial snow (rather than soil temperature) states.

The long memory of large deep soil thermal perturbations may cause significant regional impacts and teleconnections through land-atmosphere interaction and large-scale circulation (Xu et al. 2022; Xue et al. 2022). Since soil perturbations are much stronger when and where snow cover is altered, skill differences in seasonal climate prediction between EXP and CTL can be primarily attributed to changes in snow cover. As discussed below, the impacts of initial land conditions over the Tibetan and Mongolian Plateaus can continue beyond July, while those in eastern China are trivial. The impacts from the Tibetan Plateau are expected to

Accepted for publication in *Journal of Climate*. DOI 10.1175/JCLI-D-23-0565.1.

be especially large as it provides persistent heating sources elevated above 3000 meters to significantly alter continental to global circulations with teleconnections.

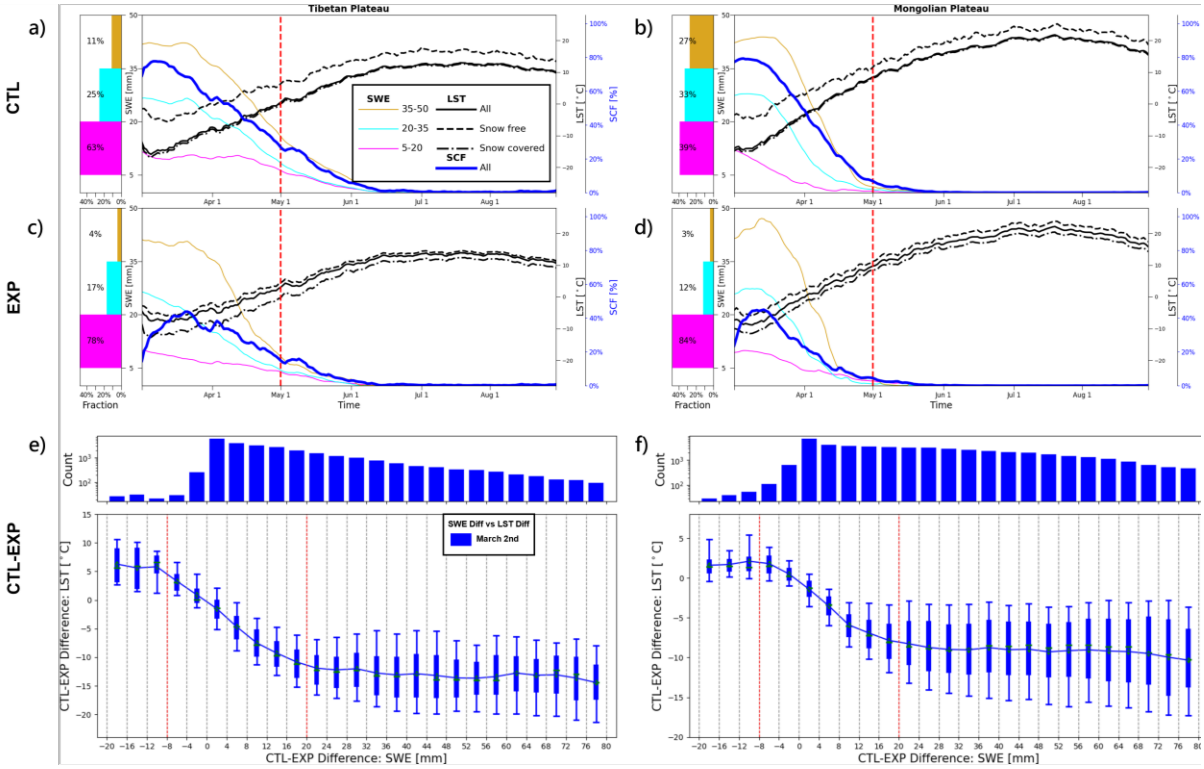

Figure 3. The proportions (left subpanel) of the initial SWE grids grouped in three ranges (50-35, 35-20, 20-5 mm) and the time evolution (right subpanel) during the entire forecast period of daily mean SWE [mm] averaged over these initially grouped grids, LST [°C] averaged over snow free, snow covered, and all grids as well as SCF [%] over all grids on the Tibetan (**a**, **c**) and Mongolian (**b**, **d**) Plateaus for CTL (**a-b**) and EXP (**c-d**). All statistics are based on averages between 1991-2014. The histogram (top subpanel) of the CTL minus EXP differences in SWE connected with the boxplot (bottom subpanel) for the corresponding differences in LST on the initial date March 2 for the Tibetan (**e**) and Mongolian (**f**) Plateaus.

It is important to distinguish the relative effects of SCF versus SWE perturbations. As depicted by Eq (1), adding more snow amount (SWE) on existing snow cover increases SNP linearly but SCF by little or much slowly. Figure 3 compares daily mean variations of total SCF, LST averages over snow-free, snow-covered and all grids, and SWE averages over the grids with initial SWE in the ranges of 50-35, 35-20, and 20-5 [mm], as well as relationships of the CTL minus EXP differences in LST versus SWE on all grids with the corresponding initial SCF differences larger than 25%. On the Tibetan Plateau, compared to EXP, CTL has 7% and 8% more grids of the thick and medium SWE ranges, and conversely 15% less grids of shallow snow (20-5 mm). As snow begins to melt in mid-spring, the thick SWE diminishes much more rapidly in EXP than CTL. The differences in LST decrease linearly with those in SWE when the latter ranges from small to medium magnitudes (between -8 and 20 mm).

Accepted for publication in *Journal of Climate*. DOI 10.1175/JCLI-D-23-0565.1.

However, this tendency saturates quickly for larger ranges, approaching a mean LST difference of 5 or -10 °C for SWE differences exceeding -8 or 20 mm. While initial thick SWE grids continue to experience longer effects due to slower meltdown, grids with small-medium SWE differences contribute the most to LST differences. Similar results, albeit with varying magnitudes, are seen on the Mongolian Plateau. Given the positive snow-albedo feedback, LST warms more over these shallow SWE grids on both Plateaus.

b. Improved Skill for Spring and Summer Predictions

1) CLIMATOLOGICAL BIASES

Figure 4 compares long-term (1991-2014) average seasonal mean T2M biases and their spatial pattern predicted by CSM, CTL, and EXP. In spring, CSM produces large systematic cold biases (2-8°C) in most regions except for warm biases along steep-slope mountain ridges and small biases in southern-southeast China. CTL also has cold biases, with much reduced magnitudes in Xinjiang and northeast China but a much enhanced magnitude in the Tibetan Plateau. These cold biases correspond to the significant LST underestimation and SCF overestimation in March (Figure 1). Since CTL is initialized directly from the CSM output, the result indicates a strong and sustained impact on seasonal climate forecasts due to the CSM's excessive snow cover on March 2. Note that observations are very rare on the Tibetan Plateau, especially in the western to central parts. Thus, the observational uncertainty in these regions is very large.

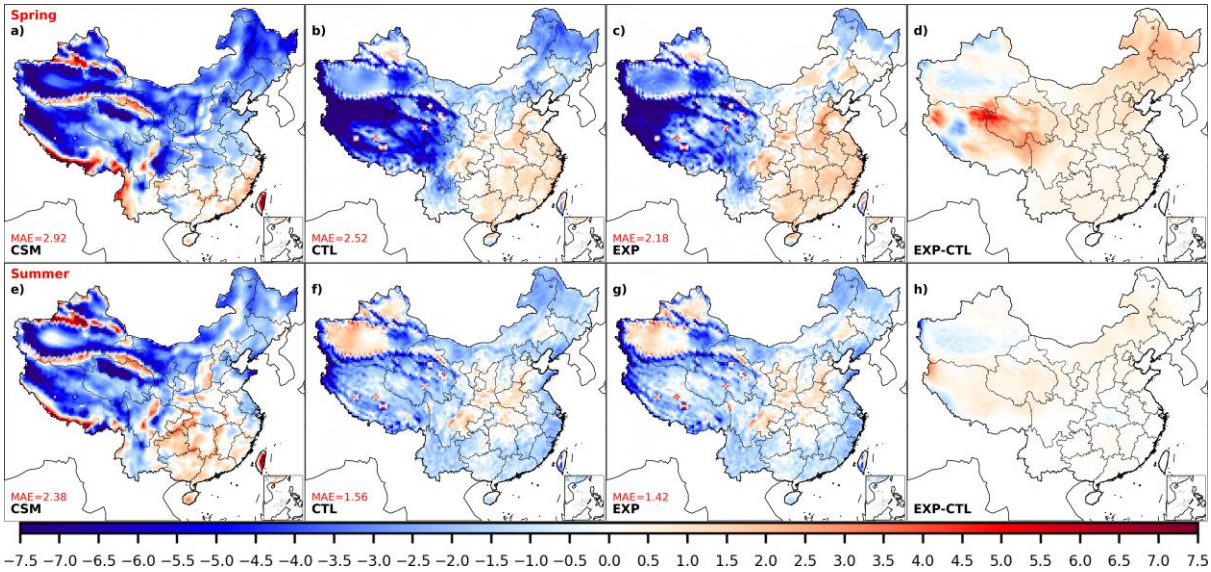

Figure 4. Geographic distributions of spring (**a-d**) and summer (**e-h**) seasonal mean biases averaged between 1991-2014 for surface air temperature (T2M [ºC]) predicted by CSM,

Accepted for publication in *Journal of Climate*. DOI 10.1175/JCLI-D-23-0565.1.

CTL, EXP, and EXP minus CTL differences. The color shaded area is statistically significant at the 5% significant level based the student's t test.

Compared with CTL, EXP predicts similar spring cold biases in the western part of the Tibetan Plateau but essentially eliminates the biases in the eastern part. EXP is also warmer than CTL in northeast China. These regions of large cold bias reduction in spring match well with the areas of warmer LST and less SCF in March (Figure 1), primarily due to the removal of initial excessive snow cover in EXP. In contrast, EXP overpredicts spring T2M in eastern China by 2.5°C on average, which is larger than 1.5°C in CTL. EXP also produces overall the lowest mean absolute errors of 2.2°C in China, as compared to 2.5°C by CTL and 2.9°C by CSM.

Summer T2M biases in all three forecast experiments decrease from spring, especially on the Tibetan Plateau in CTL and EXP. The big reduction of cold biases on the Tibetan Plateau results from snowmelt after spring due to rising temperatures. The CWRF forecasts are more similar in summer than spring, leading to closer mean absolute errors in China between 1.4°C (EXP) and 1.6°C (CTL), which are significantly reduced from 2.4°C (CSM). They share the same atmospheric forcing through lateral boundary conditions predicted by CSM. The bigger differences between CSM and CWRF suggest that the large-scale conditions play a less important role than regional processes on T2M in summer as compared to spring. In contrast, EXP in summer is still warmer than CTL by 0.5-1°C on the eastern Tibetan Plateau, which corresponds to the warmer LST and soil temperatures in March (Figure 1), indicating the persistent impact from land initialization. As discussed earlier, initial perturbations in snow cover and soil temperatures can have sustained effects into summer (Figure 2) and hence their impact on T2M remains detectable (from lateral forcing) beyond two seasons, in agreement with Xu et al. (2022).

Accepted for publication in *Journal of Climate*. DOI 10.1175/JCLI-D-23-0565.1.

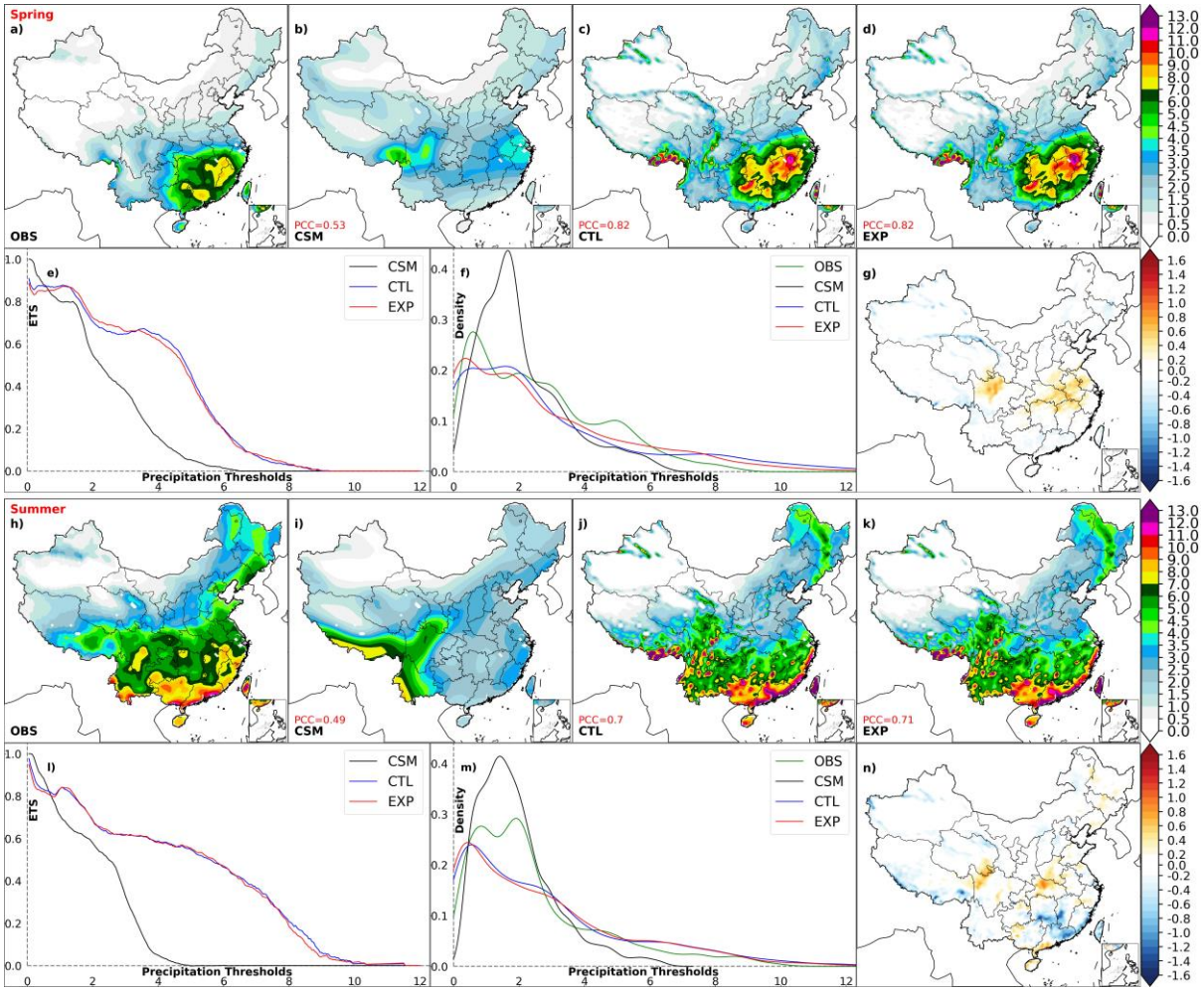

Figure 5. The geographic distributions of spring (**a-d**) and summer (**h-k**) seasonal mean precipitation (PR [mm day^{-1}]) averaged between 1991-2014 as observed (OBS) and predicted by CSM, CTL, and EXP, as well as the corresponding EXP minus CTL differences (**g, n**). The spatial pattern correlation coefficients (PCC) of predictions with observations are labeled by red on each map. Also shown are their equitable threat score **(e, l)** and kernel density **(f, m)**.

Figure 5 compares long-term seasonal mean precipitation distributions observed and predicted by CSM, CTL, and EXP. In spring, observations show two main rainbands in southeast China: immediate south of the Yangtze River and north of the Pearl River. CSM predicts poorly for not only underestimating the magnitude but also distorting the spatial distribution, having a pattern correlation with observations of only 0.53. Both CTL and EXP generally overestimate the magnitude but much better capture the spatial distribution, increasing the pattern correlation to 0.82, aligning precipitation centers more closely with observations. EXP produces 6%-20% more precipitation than CTL in the upper and lower reaches of the Yangtze River. The equitable threat score (ETS), a measure of forecast skill relative to chance (Gandin and Murphy 1992), suggests that CSM's performance deteriorates

Accepted for publication in *Journal of Climate*. DOI 10.1175/JCLI-D-23-0565.1.

quickly as rainfall surpasses approximately 2 mm day^{-1}. In contrast, CTL and EXP exhibit a significantly higher skill in predicting heavier rainfall ranging from 1 to 8 mm day^{-1}. CSM's predictions suffer from the drizzling problem, a recognized issue caused by its limited resolution (Chen et al. 2021). Specifically, CSM tends to overestimate light rainfall events but inadequately forecasts moderate to heavy rainfall. On the other hand, both CTL and EXP overestimate the heavy rainfall (>7 mm day^{-1}) coverage and maximum intensity. Note that the observational data used here are derived from rain gauges at monitoring stations coarser than the 0.25º analysis grid, most of which are located at low elevations (Liang et al. 2019). Thus, observations may likely underestimate heavy precipitation events, especially in areas with high mountains.

In summer, CSM performs even worse, with the spatial pattern correlation dropping to 0.49, as the primary rainband along the southern and eastern sides of the Tibetan plateau is incorrectly positioned and the main rainbands as observed over eastern China are absent. CTL better predicts the spatial distribution with a much higher pattern correlation of 0.70, but generally underestimates precipitation in the Yangtze River basin. EXP further improves the prediction by adding precipitation of 1 mm day^{-1} to CTL in the middle-lower reaches of the Yangtze River and subtracting a similar amount to its south - a realistic northward shift of the monsoon rainband. Given summer rainfall in eastern China decreases northward, the EXP difference from CTL accounts for up to 20-30% of total precipitation in the middle reach of the Yangtze River. Similar to spring, the summer ETS measure indicates that both CTL and EXP significantly outperform CSM in predicting most rainfall ranging from 1 to 9 mm day^{-1}. In particular, CSM demonstrates little skill for rainfall heavier than 4 mm day^{-1}, whereas CTL and EXP maintain significantly higher ETS demonstrates low skill 9 mm day^{-1}.

Both spring and summer results highlight the important skill enhancement of the CWRF downscaling prediction to the CSM operational forecasts of the climatological distributions, especially for precipitation. The CoLM-based land surface initialization largely eliminates CSM's March excessive snow cover and cold biases, especially on the Tibetan Plateau and secondary the Mongolian Plateau. This improved initialization enables EXP to predict more realistic distributions of seasonal mean surface air temperature and precipitation climatology. The result indicates that initial perturbations in snow cover and soil temperature in the highly sensitive regions can have persistent impacts on climate prediction beyond two seasons.

2) INTERANNUAL ANOMALIES

Accepted for publication in *Journal of Climate*. DOI 10.1175/JCLI-D-23-0565.1.

The spatial anomaly correlation coefficient (ACC) is commonly used in operational practice to evaluate the skill of forecasting interannual variations. It measures the spatial similarity between predicted and observed anomalies with the long-term (1991-2014) mean climatology removed. Figure 6 compares ACC interannual variation and overall statistics of T2M and precipitation predicted by CSM, CTL and EXP. For the average of all years, ACC for spring T2M prediction increases slightly from 0.18 (CSM), 0.20 (CTL) to 0.22 (EXP), indicating marginal improvements from CSM to CTL, CTL to EXP, and CSM to EXP at p-values of 0.32, 0.17, and 0.12, respectively. The average ACC for spring precipitation prediction is relatively small: 0.01 (CSM), 0.0 (CTL), and 0.02 (EXP), which differ little. Interestingly, among the ten years of relative high rainfall predictability (defined as any ACC of the three forecasts exceeding 0.2), both CTL and EXP forecasts have much higher scores than CSM in seven years (1992, 1995, 1998, 2000, 2004, 2008, 2010) with average ACC of 0.35 and 0.37 versus 0.13. In the previous winters of these years, six of them were identified with clear ENSO phases (defined as the Nino3.4 index magnitude greater than 0.5°C), indicating that CWRF can better represent regional rainfall responses to planetary circulation anomaly forcings. CSM does significantly better only in 2002 with ACC of 0.34 versus -0.26 (CTL) and -0.22 (EXP), slightly better in 1997, and almost the same in 2011.

Accepted for publication in *Journal of Climate*. DOI 10.1175/JCLI-D-23-0565.1.

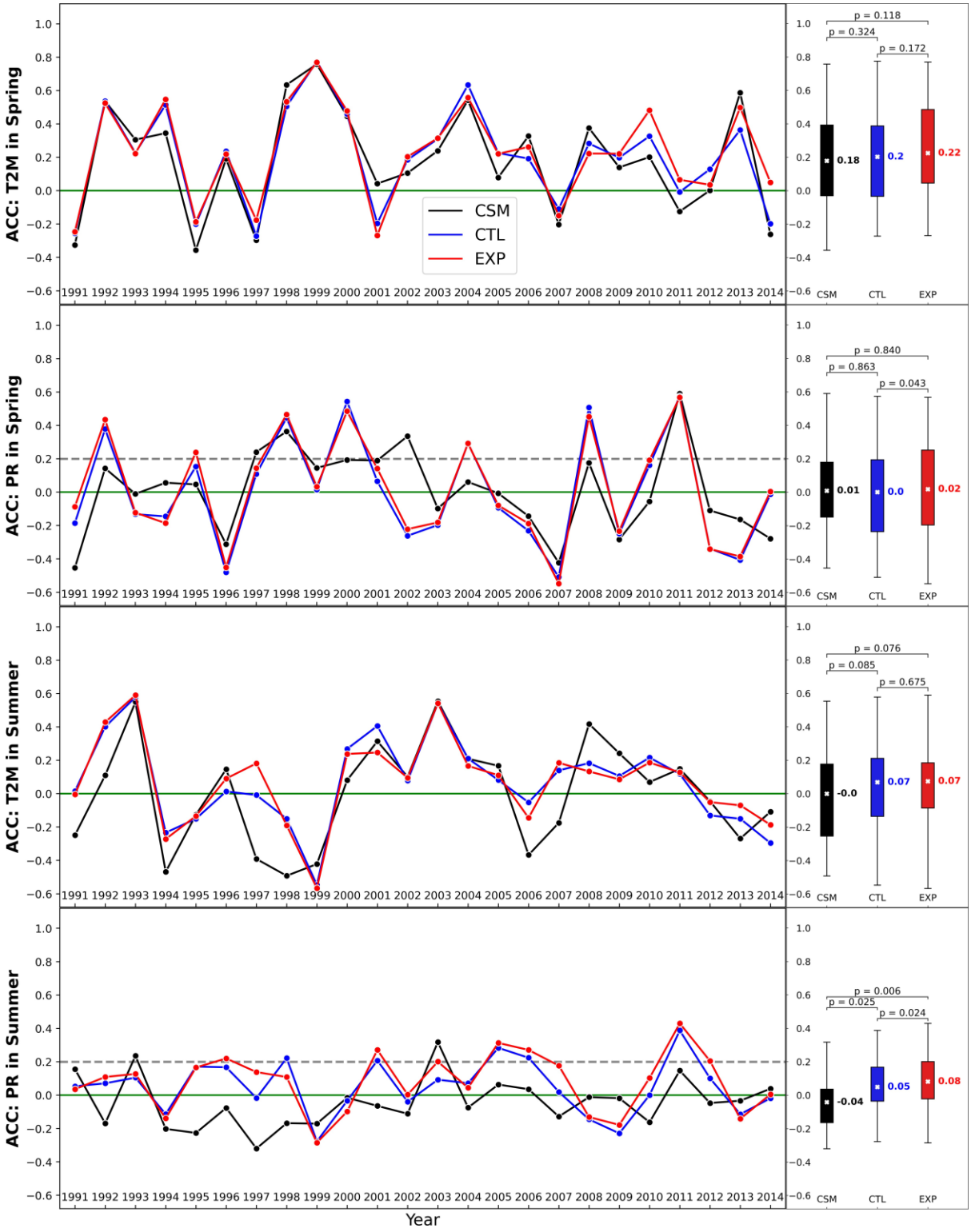

Figure 6. The spatial anomaly correlation coefficient (ACC) of predicted (CSM, CTL, EXP) with observed surface air temperature and precipitation in spring (MAM) and summer (JJA). While the left plot depicts ACC's interannual variation during 1991-2014 with a horizontal line at a threshold of 0.2 for relative high predictability, the right plot represents its interquartile range and related statistics: the mean is labeled with a cross marker; the whisker extends between the minimum and maximum; the p-value indicates the significance of the differences between two groups determined by a two-tailed paired-t-test.

Accepted for publication in *Journal of Climate*. DOI 10.1175/JCLI-D-23-0565.1.

In summer, the average ACC for T2M prediction increases from CSM (-0.0) to CTL and EXP (0.07), indicating significant improvements from CSM to CTL and EXP at p-values of 0.09 and 0.08, respectively. Both CTL and EXP improve the interquartile range, avoiding large negative ACCs in CSM. Among the ten years of high T2M predictability, CSM performs much worse than CTL and EXP in (1992, 1997, 1998, 2007), similar in (1993, 1995, 2002, 2003), but better in (2008, 2009). The average ACC for precipitation prediction increases from CSM (-0.04), CTL (0.05) to EXP (0.08), indicating significant improvements from CSM to CTL, CTL to EXP, and CSM to EXP at p-values of 0.03, 0.02, and 0.01, respectively. Among the ten years of relatively high rainfall predictability, both CTL and EXP forecasts have much higher scores than CSM in seven years (1996, 1998, 2001, 2005, 2006, 2011, 2012) with an average ACC of 0.23 and 0.26 versus -0.02; CSM did significantly better only in 2003 with an ACC of 0.32 versus 0.09 (CTL) and 0.20 (EXP) and slightly better in 1991 and 1993. CTL substantially outperforms CSM rainfall for 15 of 24 years and underperforms marginally in the rest 9 years, resulting in improved mean and interquartile range of ACCs. The improvements of EXP over CTL for precipitation are not large but consistent, with higher ACCs in 17 of 24 years.

Accepted for publication in *Journal of Climate*. DOI 10.1175/JCLI-D-23-0565.1.

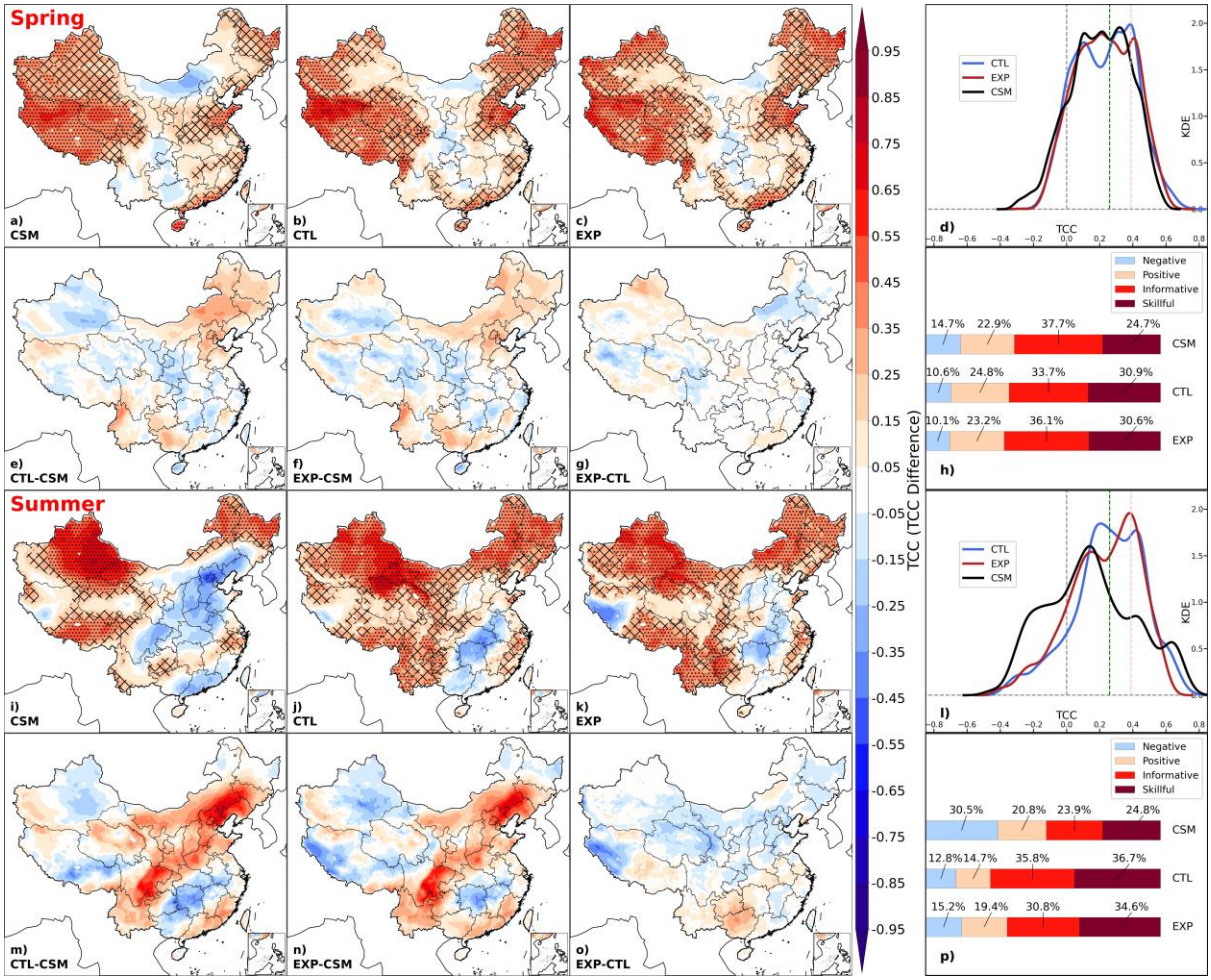

Figure 7. The interannual temporal correlation coefficient (TCC) in spring and summer during 1991-2014 between observed and predicted seasonal mean surface air temperature anomalies by CSM **(a, i)**, CTL **(b, j),** and EXP **(c, k)** as well as their differences **(e-g, m-o)**; the kernel density of TCC spatial frequency distribution **(d, l)** and the proportion of different levels of the prediction skill **(h, p)**. Dotted and crossed areas on the TCC maps **(a-c, i-k)** are statistically significant at the 5% and 20% significant level based on a one-tail student's t test, if useful TCCs are positive. Pink and green vertical lines in the kernel density indicate the TCC threshold at the 5% and 20% significant level, respectively.

Figure 7 compares the geographic distribution and kernel density of interannual temporal correlation coefficient (TCC) between observed and predicted seasonal mean T2M anomalies. Statistically significant (at p-value of 5% and 20%) positive TCCs are considered here respectively for skillful and informative forecasts, while negative TCCs indicate poor forecasts with anomalies of the wrong sign. In spring, CSM makes skillful forecasts primarily in a wide strip across the northern Tibetan Plateau to Qinghai and informative forecasts in Xinjiang. While retaining the CSM skill (with a slight degradation in Qinghai and Xinjiang), CTL achieves more significant positive TCCs in northeast and north China. CTL improves over CSM in Inner Mongolia-northeast China and southwest-southern China strips, while

Accepted for publication in *Journal of Climate*. DOI 10.1175/JCLI-D-23-0565.1.

degrading between the two strips. Overall, CTL increases the area of significant positive TCCs from CSM's 24.7% to 30.9%, while decreasing that of negative TCCs from CSM's 14.7% to 10.6%. EXP enhances CTL's TCCs in northern Xinjiang and Guangdong but reduces those in parts of northeast China, northern Tibetan Plateau, Qinghai, and Sichuan.

In summer, CSM exhibits significant positive TCCs of T2M in northern and eastern Xinjiang and across Da Hinggan Ling to Heilongjiang. While retaining these skillful regions in CSM, CTL substantially enhances the prediction in a broad band spanning southwest to northeast China and along the southeastern coast regions, increasing TCCs by 0.2-0.8. As such, CTL recovers a large area of negative TCCs in CSM and turns them to positive correlations in north and coastal south China. Overall, CTL increases the total area of skillful (informative) forecasts from CSM's 24.8% to 36.7% (23.9% to 35.8%), while decreasing that of negative TCCs from CSM's 30.5% to 12.8%. EXP slightly improves CTL in the eastern Tibetan Plateau, southwest China, and middle-lower reaches of the Yangtze River, but degrades in the southwestern Tibetan Plateau and over a wide band spanning Qinghai, Gansu, western Inner Mongolia, north China, Jilin to Heilongjiang. Thus, EXP decreases the total area of skillful forecasts by 2.1% from CTL but still increases that by 9.8% from CSM. Comparing the kernel density, CTL and EXP avoid CSM's large proportion of negative TCCs and increase the proportion of positive TCCs between 0.1-0.5, exhibiting an improved distribution.

Accepted for publication in *Journal of Climate*. DOI 10.1175/JCLI-D-23-0565.1.

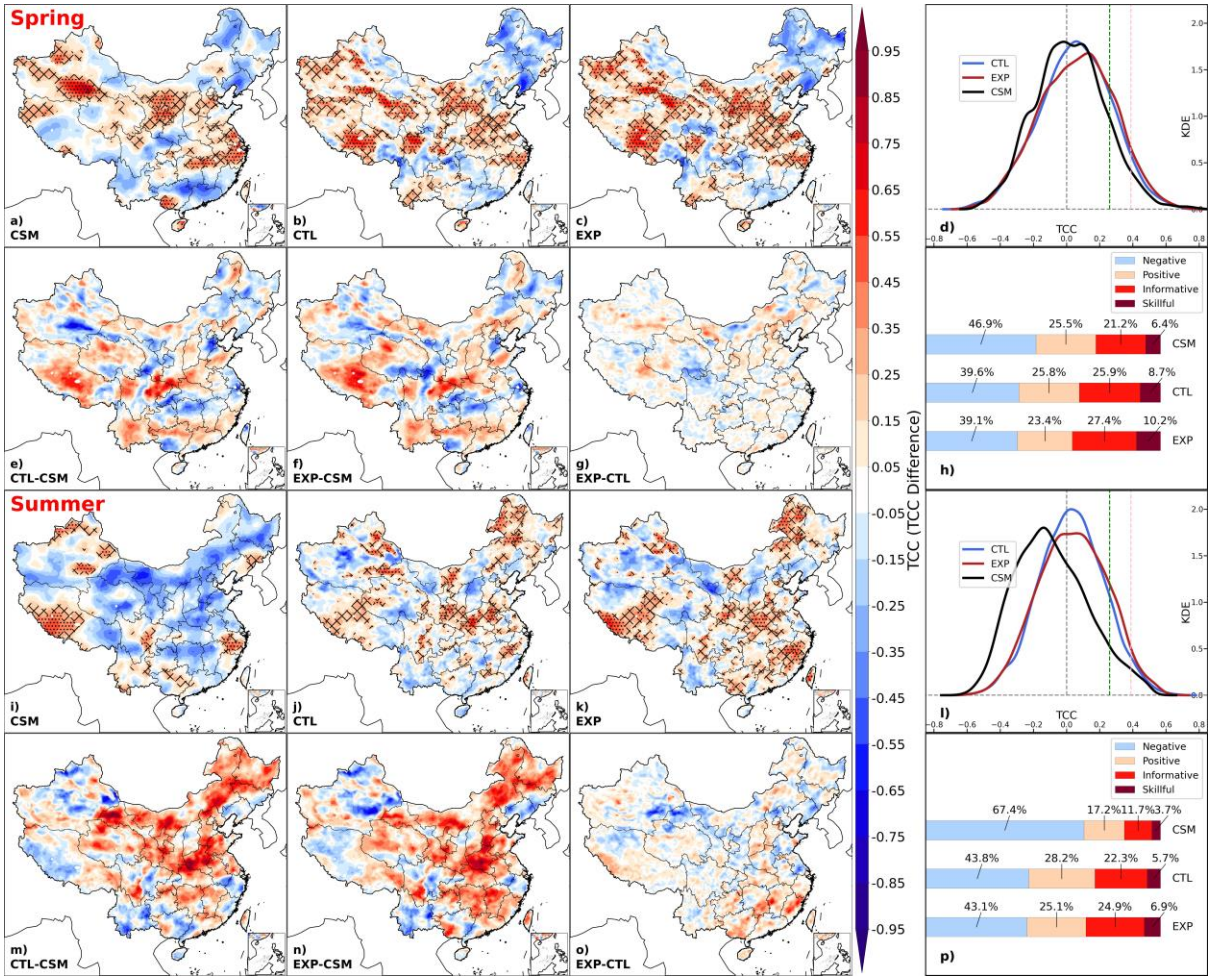

Figure 8. Same as Figure 7 except for precipitation.

Figure 8 compares the geographic distribution and kernel density of TCC between observed and predicted seasonal mean precipitation anomalies. In spring, CSM exhibits significant positive TCCs in limited areas of the Yangtze River Basin, Xinjiang, Ningxia, and Guangxi. Overall, CSM captures only 6.4% (21.2%) area with skillful (informative) forecasts, producing negative TCCs over 46.9% of China. While retaining these CSM's skillful regions, CTL largely increases TCCs in the Tibetan Plateau and along Sichuan to Henan and Yunnan to the Perl River basin, where CSM produces generally large negative correlations. As such, CTL increases from CSM the total area of skillful forecasts by 2.3% while reducing that of negative TCCs by 7.3%. EXP skill is comparable to CTL, with a marginal increase of the skillful area by 1.5%. Comparing the kernel density, EXP shows the highest proportion among TCCs from the thresholds for informative and skillful forecasts to 0.6, surpassing CTL slightly and CSM by a larger margin.

In summer, CSM has skillful rainfall forecasts in limited areas of Zhejiang, eastern Xinjiang, southwestern Tibetan Plateau, and eastern Sichuan, while producing negative TCCs

Accepted for publication in *Journal of Climate*. DOI 10.1175/JCLI-D-23-0565.1.

over 67.4% of China. CTL greatly enhances TCCs over most regions in central and eastern China, where CSM shows extensive negative correlations. Corresponding to the systematic bias reduction (Figure 5), CTL reduces the total area of negative TCCs by 23.6% and increases the area of informative and skillful forecasts respectively by 10.6% and 2.0%, highlighting the added value of CWRF downscaling. EXP further refines CTL in south China and the Yangtze River basin with more organized and larger positive TCCs, increasing the area of informative and skillful forecasts respectively by 2.6% and 1.2%. Notably, these skill enhancements by CTL and EXP occur mostly over the primary rainbands associated with the summer East Asian monsoon. The systematic TCC increases in broad areas are likely caused by CWRF's improved (over CSM) representation of key physical processes that enable more realistic capture of regional precipitation responses to large-scale circulation anomalies.

4. Process Understanding

Identifying and comprehending the physical mechanisms responsible for variations in climate predictive skill among different forecast models remains a significant challenge. In this section, we aim to explore the key processes that are associated with skill enhancement through CWRF downscaling and land initialization. Both CTL and EXP forecasts are driven by the same planetary circulation forcings as CSM, particularly in the upper troposphere, through CWRF's dynamic relaxation of lateral boundary conditions across the buffer zones (Liang et al. 2001). Consequently, forecast disparities within the CWRF computational domain stem from differences in how the models represent regional processes due to variations in resolution, physics, and initialization. By conducting this analysis, we hope to gain valuable insights into potential avenues for enhancing the climate predictive skill.

Accepted for publication in *Journal of Climate*. DOI 10.1175/JCLI-D-23-0565.1.

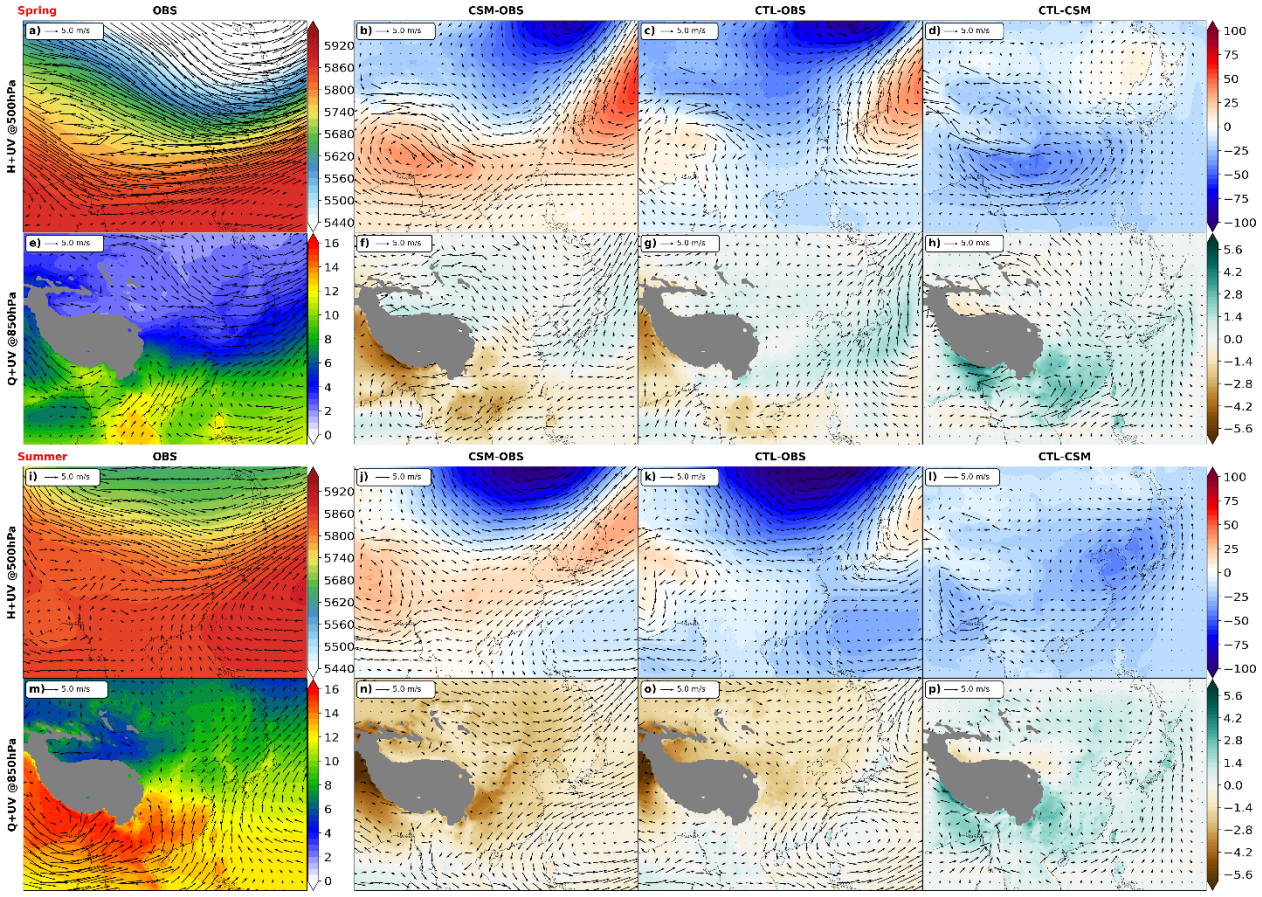

Figure 9. Seasonal mean distributions averaged between 1991-2014 for observed (OBS) spring (**a**) geopotential height ([gpm], color shading) overlaid with wind ([m s^{-1}], vector) at 500hPa and (**e**) specific humidity ([g kg^{-1}], color shading) with wind ([m s^{-1}], vector) at 850hPa, and their respective CSM (**b, f**) and CTL (**c, g**) biases, as well as CTL minus CSM differences (**d, h**). The corresponding summer distributions are shown in (**i, m, j, n, k, o, i, p**).

Figures 9 and S2 show the observed seasonal mean circulation characteristics and compare the CSM and CTL predicted biases as well as their differences at 850hPa, 500hPa, and 200hPa. In spring, observations at 500hPa reveal two dominant westerly branches, which are divided by the mechanical blocking effect of the Tibetan Plateau. As a result of this separation, two troughs form: one located over Northeast China and Eastern Siberia, and another on the southern side of the Tibetan Plateau. Due to its coarse resolution, CSM smooths high terrains, allowing more air flow to climb over the Plateau and causing a northward shift of the southern branch. The shift strengthens the westerlies from Xinjiang to Northeast China while weakening them in the south of the Plateau. This causes geopotential height to decrease on the northern side of the westerly jet stream, leading to the westward displacement of the East Asian trough. Simultaneously, the southern side experiences increased geopotential height across the Plateau's south foothill to South China, resulting in a

Accepted for publication in *Journal of Climate*. DOI 10.1175/JCLI-D-23-0565.1.

decreased pressure gradient from the Indian Ocean and South China Sea inland, which inhibits low-level water vapor transport. Consequently, CSM produces dry biases at 850hPa and substantially underestimates precipitation across entire Central to South China (Figure 5). In contrast, CWRF with an improved physics representation at a finer resolution (Liang et al. 2019) more effectively captures the Plateau's blocking and thermal effects, preventing the northward shift of the southern branch and rectifying the geopotential height overestimation. However, the CTL predicted geopotential height still exhibits notable underestimates in Mongolia to East Siberia and overestimates in the Sea of Japan. These biases resemble CSM with reduced magnitudes and result from lateral boundary conditions. Nevertheless, the CTL's corrected southern trough reduces overall geopotential height overestimation and guides the south-westerlies beneath it to transport more water vapor inland, resulting in more realistic rainfall across Central to South China.

In summer, the observed 500hPa westerlies decelerate, and merge into one jet stream - EAJ, which shifts northward compared to spring. Consequently, the WPSH strengthens and moves over the northwestern Pacific Ocean. Stronger southerlies at 850hPa transport more water vapor from the Indian Ocean and the South China Sea inland, providing abundant moisture for summer East Asian monsoon rainfall. CSM continues to overestimate westerlies from Xinjiang to the Northeast. A stronger EAJ further lowers the geopotential height on its left side over East Siberia and raises it on its right side over the Sea of Japan, weakening and shifting the WPSH northwards. As a result, CSM significantly underestimates 850hPa southerlies in South China, leading to a considerable decrease in moisture transport from the South China Sea inland and causing substantial rainfall deficits across entire Central to South China (Figure 5). The general patterns of these CSM biases resemble each other between summer and spring. Under the influence of lateral boundary conditions from CSM, CTL inherits the overprediction of the EAJ and East Asian trough in the upper troposphere from the northern buffer zone while experiencing insufficient 850hPa southerlies from the southern buffer zone. These errors contribute to the underestimated rainfall in Central and North China, as the weakened southerlies in South China decrease the meridional water supply to the Yangtze River basin and North China. On the other hand, CTL notably reduces the overestimation of the upper-level westerlies from Xinjiang to the Northeast and the underestimation of the lower-level southwesterlies across the Indian Ocean to the South China Sea. Partly because the latter brings more sustained moisture flux from the Indian-Indochina Peninsula, CTL more accurately captures the summer monsoon rainbands across

Accepted for publication in *Journal of Climate*. DOI 10.1175/JCLI-D-23-0565.1.

South to Central China. In addition to the increased resolution, CTL's enhancement in rainfall skill is critically attributed to its improved physics representations (Liang et al. 2019).

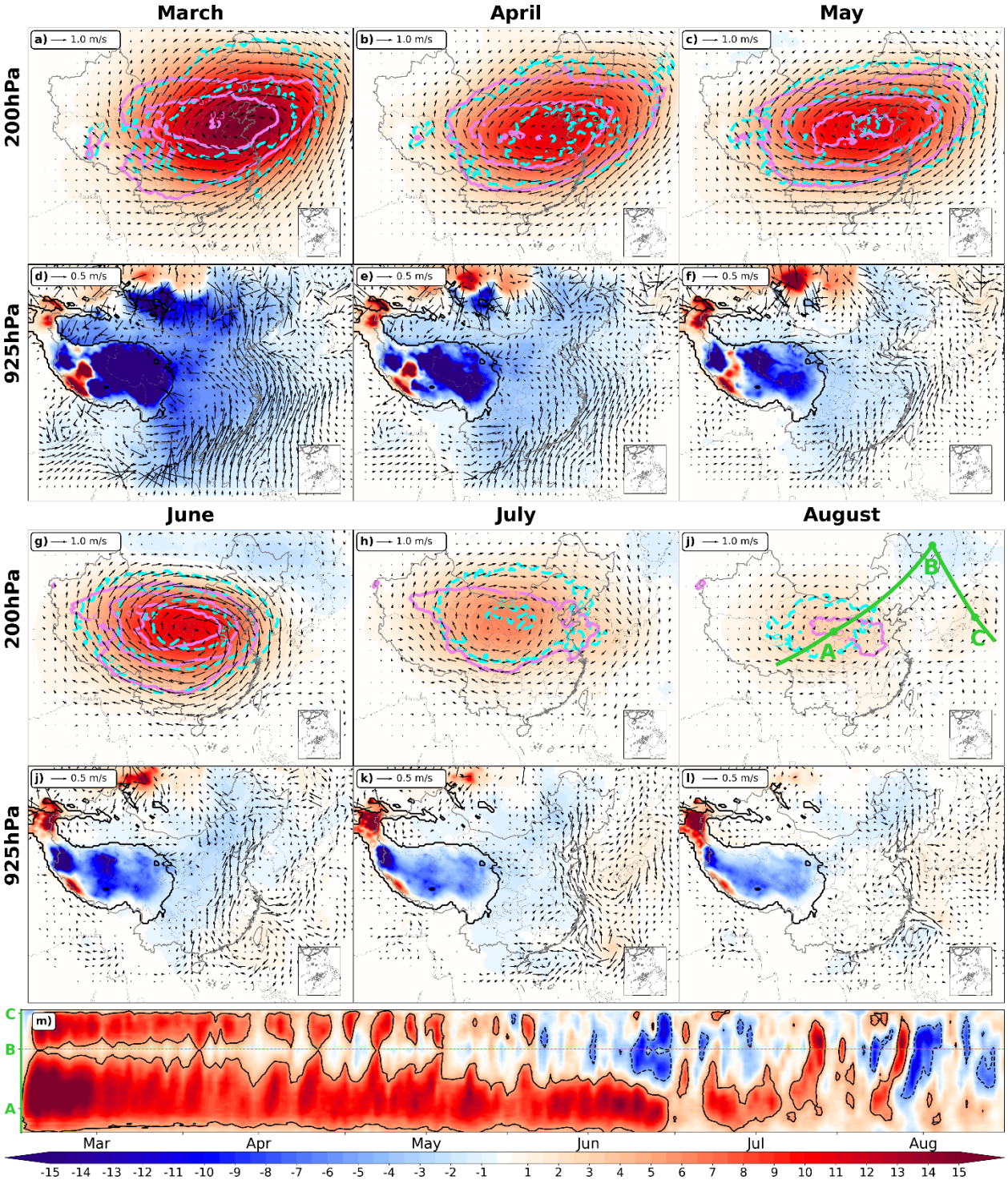

Figure 10. March to August monthly mean distributions of EXP minus CTL differences in geopotential height ([gpm], color shading) and wind ([m s^{-1}], vector) at 200hPa (**a-c**, **g-j**) and 925hPa (**d-f**, **j-l**), as well as daily variations of the geopotential height differences (**m**) along the A-B-C route marked on **(j)**. The purple and cyan contours show the corresponding temperature differences [ºC] at respectively 300hPa and 100hPa with intervals of 0.1 ºC.

Accepted for publication in *Journal of Climate*. DOI 10.1175/JCLI-D-23-0565.1.

Figure 10 depicts the temporal evolution and spatial distribution of the major circulation differences resulting from substituting the land initialization in EXP using the observation-CoLM integration compared to CTL using the CSM direct output. In EXP, the reduction of excessive snow cover over the Tibetan Plateau and across Mongolia-Northeast China causes localized heating within an expanded vertical column. As a result, the geopotential height increases in the upper layers and decreases in the lower layers. This leads to a perturbation of an anticyclonic geostrophic circulation in the upper troposphere, creating a warming center near 200hPa and a cooling center in the lower stratosphere. The finding aligns with earlier theoretical studies (Hoskins and Karoly 1981). At the same time, a perturbated cyclonic circulation develops in the lower troposphere, leading to the reinforcement of southerly winds at 925hPa across the South China Sea and eastern China's coastal areas. This circulation pattern transports more moisture northward, causing a decrease in precipitation in South China but an increase in the Yangtze River basin in both spring and summer (Figure 5g,n).

These circulation perturbations are most prominent in March and gradually diminish in August. From the daily average along a cross-section from the Tibetan Plateau to Northeast China and extending to the Sea of Japan (Figure 10m), we observe distinctive Rossby wave patterns in the 200hPa geopotential height perturbations. Initially, these waves exhibit oscillation in a northern expansion, progressing toward Northeast China, with the center magnitude weakening as they approach the Yellow River's Hetao region and North China. This trend continues until early June, when a negative geopotential height perturbation center forms over the Sea of Japan. Subsequently, the dipole oscillation structure strengthens until the end of June, followed by a gradual weakening until mid-July, during which the Rossby waves demonstrate an even clearer eastward propagation in summer. Accompanying this wave activity, the SAH is intensified and the EAJ is shifted northward. Consequently, this leads to the strengthening of southerly winds in eastern China and a northward shift of rain bands. These findings are consistent with Wang et al. (2014), Xu et al. (2022) and Xue et al. (2022), who found that introducing anomalous heating perturbations through increasing initial soil temperatures in the Tibetan Plateau can produce similar changes in the SAH, EAJ, and Rossby wave activity. The forcing-response pattern is a regional presentation of the Tibetan Plateau-Rocky Mountain Circumglobal (TRC) wave train named by Xue et al. (2023). Given the transient nature of Rossby waves, the associated disturbances may not line up perfectly among years. However, the consistent propagation path of similar characteristics contributes to a detectable signal in the long-term average, underlining the significant

Accepted for publication in *Journal of Climate*. DOI 10.1175/JCLI-D-23-0565.1.

influence of initial snow perturbations over the Tibetan Plateau on atmospheric circulation patterns and consequently regional climate conditions in eastern China.

Index	**SAHI**	**EAJI**	**TROI**	**WPSHI**	**V850I**
CSM	0.45*	0.42*	0.34	0.53**	-0.15
CTL	0.61**	**0.43***	**0.44***	0.55**	0.36
EXP	**0.63****	**0.43***	0.42*	**0.58****	**0.38**

Table 2. The temporal correlation coefficients between predicted and observed interannual variations of summer regional mean circulation indices SAHI, EAJI, TROI, WPSHI, and V850I, comparing CSM, CTL, and EXP forecasts. The regional boundaries for these indices are shown in Figure 11b-e. The highest value among the three forecasts for each index is bolded. Statistically significant values at the 5% and 1% significance levels by student's t-test are depicted by a single (*) and double (**) asterisk, respectively.

As elaborated above, significant differences in performance can be observed among CSM, CTL, and EXP forecasts when reproducing climatological (1991-2014) mean characteristics. These differences are more pronounced in spring than in summer, evident in both regional forcing factors and local to remote responses, as depicted in Figures 1-5 and identified with key physical processes in Figures 9-10. In contrast, the disparities in skill for capturing observed interannual anomalies are notably smaller during spring compared to summer, particularly for remote responses in eastern China, as shown in Figures 6-8. Despite the challenges in identifying underlying mechanisms for the differences, our focus remains on understanding the relatively large signals in forecasting summer interannual anomalies.

Accepted for publication in *Journal of Climate*. DOI 10.1175/JCLI-D-23-0565.1.

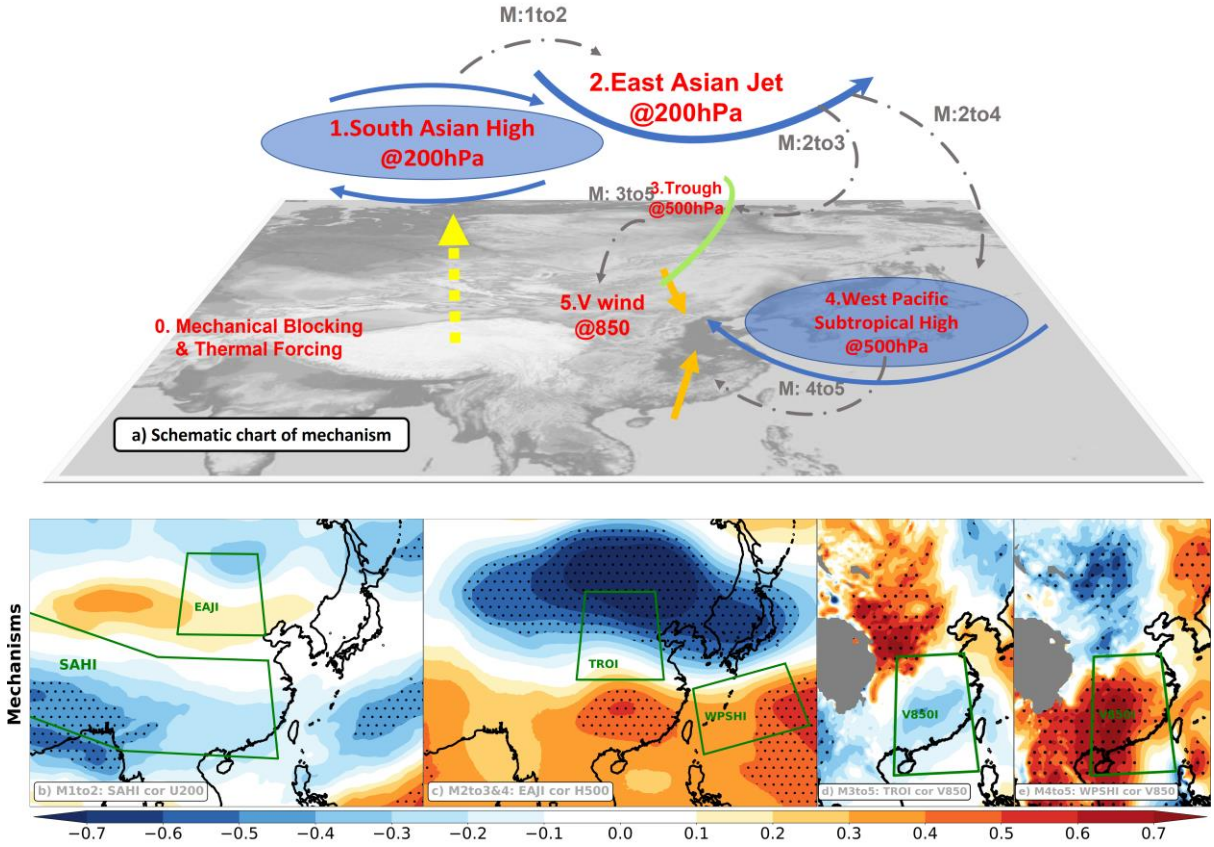

Figure 11. The possible mechanisms between Tibetan Plateau's mechanical and thermal forcing to regional circulation anomalies in summer. (**a**) the schematic of the mechanisms; (**b**) Mechanism 1 to 2: geographic distribution of temporal correlation between 200hPa zonal wind (U200) and the South Asian High index (SAHi) calculated with ERA5. Dotted areas are statistically significant at the 5% significance level based on a student's t test. The SAHi is defined averaged geopotential in the lower green polygon. (**c**) Mechanism 2 to 3&4: Same as (b), except for TCC between 500hPa geopotential (H500) and the East Asian Jet index (EAJi) defined in (b). (**d**) Mechanism 3 to 5: Same as (b), except for TCC between 500hPa trough index (TROi) and 850hPa meridional wind (V850). (**e**) Mechanism 4 to 5: Same as (b) except for TCC between the Western Pacific Subtropical High index (WPSHi) and V850.

Figure 11 illustrates the possible mechanisms and associated processes that explain the CWRF downscaling advantage over CSM in predicting interannual anomalies of summer precipitation in eastern China. CWRF demonstrates an improved representation of the Tibetan Plateau's mechanical blocking and thermal forcing effects, leading to an intensified SAH and an accelerated EAJ on its northern flank (Figure 11b). The intensified upper-level divergence to the left of the EAJ exit decreases 500hPa geopotential height, strengthening the East Asian trough over the Hetao region, while the intensified convergence to the right strengthens the WPSH (Figure 11c). Consequently, the stronger East Asian trough guides more low-level cold air from high latitudes to Central China (Figure 11d), while the stronger WPSH steers more southerly winds with increased moisture transport from lower latitudes

Accepted for publication in *Journal of Climate*. DOI 10.1175/JCLI-D-23-0565.1.

(Figure 11e). CWRF more realistically captures the converging air masses, leading to increased rainfall in eastern China, especially over the Central to Northeast regions, compared to CSM. Specifically, CTL increases TCCs with observed 200hPa westerly winds by 0.3 between the Yangtze and Yellow Rivers and 850hPa southerly winds by 0.6 in Southeast China. This leads to obvious improvements in 500hPa vertical motion (Figure 12c) and 1000-500hPa column moisture convergence (Figure 12d) across Central to North China. EXP predicts even higher TCCs with observations than CTL for southerly winds along the Yangtze River (Figure 12f), as well as vertical motion (Figure 12g) and moisture convergence (Figure 12h) in many areas of eastern China. Consequently, EXP shows a higher skill in predicting interannual anomalies of summer rainfall in eastern China compared to CTL.

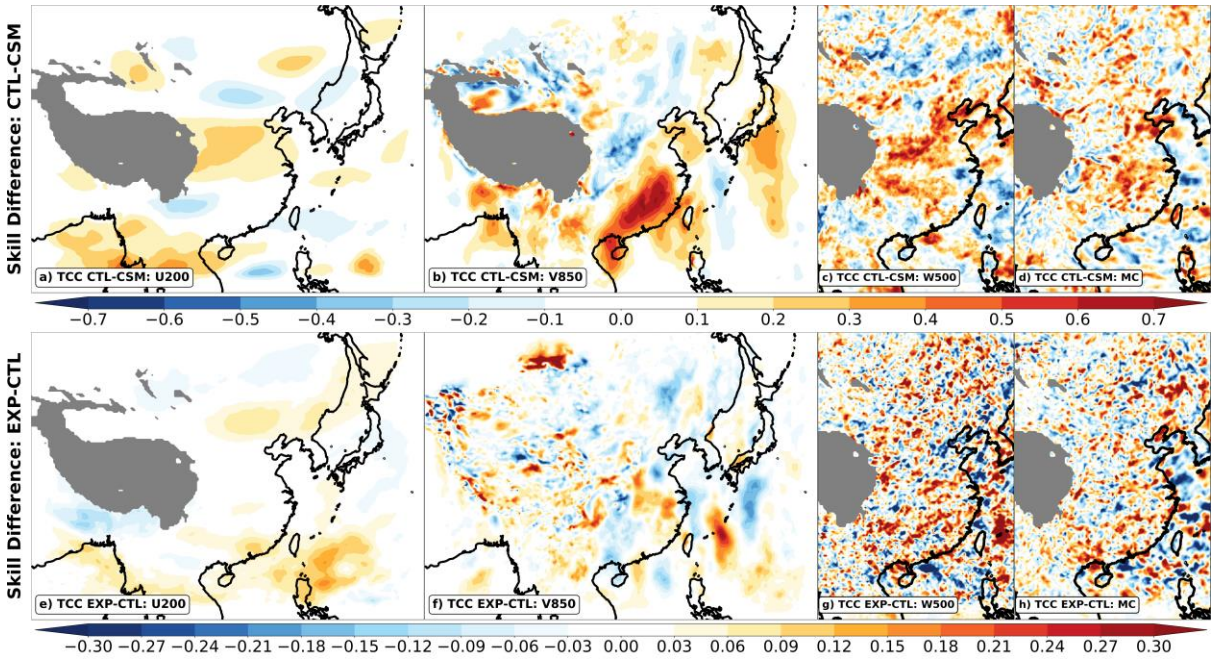

Figure 12. (**a-d**) CTL minus CSM differences of the TCC skill in predicting 200hPa zonal wind (U200), 850hPa meridional wind (V850), 500hPa vertical velocity (W500), and moisture convergence (MC) integrated from 1000hPa to 500hPa. (**e-h**) same as (a-d), except for EXP minus CTL skill differences.

Table 2 compares the TCCs of interannual anomalies of predicted regional circulation indices with observations during the summer. Both CTL and EXP outperform CSM for all indices, with particularly significant skill gains identified for SAH and V850 indices. CTL increases TCC from CSM by 0.16 for SAH and 0.51 for V850, while EXP increases are 0.18 and 0.53, respectively. These consistent results demonstrate the systematic improvements of

Accepted for publication in *Journal of Climate*. DOI 10.1175/JCLI-D-23-0565.1.

CWRF downscaling over CSM predictions, spanning from synoptic-mesoscale circulations to regional precipitation processes.

5. Summary and Conclusions

This study evaluates the skill enhancement of CWRF downscaling and land initialization from CSM operational seasonal forecasts in China and identifies the key mechanisms underlying the improvements. All CSM and CWRF forecasts are initialized each year on March 2 and end on August 31 from 1991 to 2014. As driven by time-varying lateral boundary conditions from the CSM forecast, two parallel CWRF downscaling forecasts are conducted, differing only in land initialization. The CWRF control (CTL) forecast uses initial atmospheric and land conditions directly from the CSM forecast, while its experiment (EXP) forecast substitutes initial land conditions from a standalone CoLM long integration driven by the observational reanalysis.

The comparison demonstrates that CWRF downscaling significantly reduces CSM's regional climate biases in surface air temperature and precipitation in both spring and summer. The bias reduction is particularly substantial for precipitation, increasing the spatial pattern correlation with observations in China from 0.53 to 0.82 in spring and from 0.49 to 0.70 in summer. For both seasons, CSM totally misses the main rainbands in South and Central China and produces a severe drizzling problem, while CWRF realistically restores these rainbands and improves moderate to heavy (larger than 1 mm day^{-1}) rainfall with much higher ETS scores. Compared to CTL, EXP largely reduces excessive snow cover over the Tibetan Plateau and across Mongolia-Northeast China and hence essentially eliminates large cold biases there. The forecast circulation responses to the initialization correction are most prominent in March and gradually diminish in August. As a result, EXP reduces CTL's dry biases in the Yangtze River basin in both spring and summer, with a realistic northward shift of the summer monsoon rainband.

CWRF downscaling also significantly enhances CSM's predictive capabilities for interannual anomalies in surface air temperature and precipitation over China mainland. The downscaling increases the factional area of skillful forecasts (defined as positive TCCs exceeding the 5% significance level) by 6.2% in spring and 11.9% in summer for temperature, and by 2.3% in spring and 2.0% in summer for precipitation. Moreover, the downscaling reduces the area of negative TCCs (anomalies of the wrong sign) by 4.1% in

Accepted for publication in *Journal of Climate*. DOI 10.1175/JCLI-D-23-0565.1.

spring and 17.7% in summer for temperature, and by 7.3% in spring and 23.6% in summer for precipitation. Especially for precipitation prediction, the downscaling achieves markedly higher scores in seven out of the ten years with relatively high predictability (defined as any ACC of the three forecasts exceeding 0.2). On average, there is an average ACC increase of 0.22 in spring and 0.25 in summer, indicating substantial enhancements in predictive accuracy of seasonal rainfall anomaly patterns during these years. While the improvements of EXP over CTL for precipitation anomaly prediction are modest, they show consistency, with higher summer ACC in 17 out of 24 years.

The predictive skill enhancements by CWRF downscaling can be linked to notable improvements in the representation of key physical processes governing surface air temperature and precipitation spatiotemporal variations across China. By employing an improved physics representation at a finer resolution, CWRF more accurately captures the complex interactions of the Tibetan Plateau's blocking and thermal effects, as well as their teleconnection patterns over China. Consequently, the downscaling depicts more realistic SAH, EAJ, and WPSH circulation systems. These systems play a crucial role in determining regional temperature and precipitation distributions, particularly in eastern China where they jointly affect the weather patterns. Especially during summer, CTL shows notable advancements over CSM. It predicts an intensified SAH with an accelerated EAJ on its northern flank and a strengthened WPSH downstream. As a result, the CTL circulations steer more cold air from high latitudes and facilitate enhanced moisture transport from lower latitudes with stronger southerly winds. The more realistic representation of these converging air masses in CTL leads to increased rainfall in eastern China, particularly over the central to northeast regions, with a much more accurate prediction of mean distributions and interannual anomalies than CSM.

Similar circulation processes can be identified for the skill enhancements of EXP over CTL. The integration of observations in the CoLM substantially reduces excessive snow cover and cold soil biases in the initial land conditions. Especially on the Tibetan Plateau, EXP shows persistently lower snow cover until early June, while its warmer soil temperature perturbations continue throughout March to August. This improved initialization leads to localized heating within an expanded vertical column, enabling EXP to more realistically predict intensified SAH and WPSH circulation systems. Consequently, the intensification results in reinforced southerly winds across the South China Sea and eastern China's coastal

Accepted for publication in *Journal of Climate*. DOI 10.1175/JCLI-D-23-0565.1.

areas. This circulation pattern transports more moisture northward, causing a realistic northward shift of the summer monsoon rainband, compared to CTL. The results indicate that initial perturbations in snow cover and soil temperature within highly sensitive regions can have persistent impacts on climate predictions for periods extending beyond two seasons. Furthermore, these impacts may be more significant and manifest with a delay in remote regions, facilitated by Rossby wave propagations and teleconnection patterns.

In conclusion, this study highlights the advancements achieved in seasonal climate predictions through CWRF downscaling and enhanced land initialization. However, it is essential to acknowledge that the predictive skill of interannual climate anomalies in China remains unsatisfactory (Wang et al. 2022). As we move forward, it becomes increasingly imperative to pursue further refinements in both global and regional models while embracing the integration of land-atmosphere-ocean coupled data assimilation systems. By committing to these avenues of research, we can pave the way for more accurate and robust climate predictions at regional scales, offering longer lead times and enhancing our understanding and preparedness to address challenges posed by climate anomalies and extremes.

Acknowledgments.

This research was supported by National Natural Science Foundation of China under grant agreement numbers 42088101 and the U.S. National Science Foundation Innovations at the Nexus of Food, Energy and Water Systems under Grant EAR1903249. The simulations and analyses were conducted on clusters in the national climate center of the China Meteorological Administration.

Data Availability Statement.

All BCC_CSM and CWRF experiments' outputs used to generate the analyses in the manuscript are available from the corresponding authors upon request.

REFERENCES

Ambroise, B., K. Beven, and J. Freer, 1996: Toward a generalization of the TOPMODEL concepts: Topographic indices of hydrological similarity. Water Resour. Res., 32, 2135-2145, https://doi.org/10.1029/95WR03716.

Accepted for publication in *Journal of Climate*. DOI 10.1175/JCLI-D-23-0565.1.

Beven, K. J., and M. J. Kirkby, 1979: A physically based, variable contributing area model of basin hydrology. Hydrological Sciences Bulletin, 24, 43-69, https://doi.org/10.1080/02626667909491834.

Bonan, G., 1996: A Land Surface Model (LSM Version 1.0) for Ecological, Hydrological, and Atmospheric Studies: Technical Description and User's Guide (No. NCAR/TN-417+STR). University Corporation for Atmospheric Research. http://dx.doi.org/10.5065/D6DF6P5X

Broxton, P. D., X. Zeng, and N. Dawson, 2017: The Impact of a Low Bias in Snow Water Equivalent Initialization on CFS Seasonal Forecasts. J. Climate, 30, 8657-8671, https://doi.org/10.1175/JCLI-D-17-0072.1.

Chen, D., A. Dai, and A. Hall, 2021: The convective-to-total precipitation ratio and the "Drizzling" Bias in Climate Models. J. Geophys. Res. Atmos., 126, e2020JD034198, https://doi.org/10.1029/2020JD034198.

Chen, L., X.-Z. Liang, D. DeWitt, A. N. Samel, and J. X. L. Wang, 2016: Simulation of seasonal US precipitation and temperature by the nested CWRF-ECHAM system. Climate Dyn., 46, 879-896, https://doi.org/10.1007/s00382-015-2619-9.

Choi, H. I., and X.-Z. Liang, 2010: Improved Terrestrial Hydrologic Representation in Mesoscale Land Surface Models. J. Hydrometeor., 11, 797-809, https://doi.org/10.1175/2010JHM1221.1.

——, P. Kumar, and X.-Z. Liang, 2007: Three-dimensional volume-averaged soil moisture transport model with a scalable parameterization of subgrid topographic variability. Water Resour. Res., 43, W04414, https://doi.org/10.1029/2006WR005134.

Choi, H. I., X.-Z. Liang, and P. Kumar, 2013: A Conjunctive Surface-Subsurface Flow Representation for Mesoscale Land Surface Models. J. Hydrometeor., 14, 1421-1442, https://doi.org/10.1175/JHM-D-12-0168.1.

Chou, M.-D., and M. J. Suarez, 1999: A solar radiation parameterization for atmospheric studies (No. NASA/TM-1999-104606/VOL15), https://ntrs.nasa.gov/citations/19990060930.

Accepted for publication in *Journal of Climate*. DOI 10.1175/JCLI-D-23-0565.1.

——, ——, X.-Z. Liang, M. M.-H. Yan, and C. Cote, 2001: A thermal infrared radiation parameterization for atmospheric studies, (No. NASA/TM-2001-104606/VOL19), https://ntrs.nasa.gov/citations/20010072848.

Coakley, J. A., and P. Chylek, 1975: Two-Stream Approximation in Radiative Transfer: Including the Angle of the Incident Radiation. J. Atmos. Sci., 32, 409-418, https://doi.org/10.1175/1520-0469(1975)032<0409:TTSAIR>2.0.CO;2.

Cocke, S., T. E. LaRow, and D. W. Shin, 2007: Seasonal rainfall predictions over the southeast United States using the Florida State University nested regional spectral model. J. Geophys. Res. Atmos., 112, D04106, https://doi.org/10.1029/2006JD007535.

Dai, Y., and Q. Zeng, 1997: A land surface model (IAP94) for climate studies part I: Formulation and validation in off-line experiments. Adv. Atmos. Sci., 14, 433-460, https://doi.org/10.1007/s00376-997-0063-4.

——, F. Xue, and Q. Zeng, 1998: A land surface model (IAP94) for climate studies part II: Implementation and preliminary results of coupled model with IAP GCM. Adv. Atmos. Sci., 15, 47-62, https://doi.org/10.1007/s00376-998-0017-5.

——, and Coauthors, 2003: The Common Land Model. Bull. Amer. Meteor. Soc., 84, 1013-1024, https://doi.org/10.1175/BAMS-84-8-1013.

——, R. E. Dickinson, and Y.-P. Wang, 2004: A Two-Big-Leaf Model for Canopy Temperature, Photosynthesis, and Stomatal Conductance. J. Climate, 17, 2281-2299, https://doi.org/10.1175/1520-0442(2004)017<2281:ATMFCT>2.0.CO;2.

De Sales, F., and Y. Xue, 2006: Investigation of seasonal prediction of the South American regional climate using the nested model system. J. Geophys. Res. Atmos., 111, D20107, https://doi.org/10.1029/2005JD006989.

Dickinson, R. E., A. Henderson-Sellers, and P. J. Kennedy, 1993: Biosphere-Atmosphere Transfer Scheme (BATS) version le as coupled to the NCAR community climate model. Technical note. [NCAR (National Center for Atmospheric Research)]. https://www.osti.gov/biblio/5733868.

Diez, E., B. Orfila, M. D. Frias, J. Fernandez, A. S. Cofino, and J. M. Gutierrez, 2011: Downscaling ECMWF seasonal precipitation forecasts in Europe using the RCA model.

Accepted for publication in *Journal of Climate*. DOI 10.1175/JCLI-D-23-0565.1.

Tellus Ser. A-Dyn. Meteorol. Oceanol., 63, 757-762, https://doi.org/10.1111/j.1600-0870.2011.00523.x.

Diffenbaugh, N. S., J. S. Pal, R. J. Trapp, and F. Giorgi, 2005: Fine-scale processes regulate the response of extreme events to global climate change. Proc. Natl. Acad. Sci. U.S.A., 102, 15774-15778, https://doi.org/10.1073/pnas.0506042102.

Ding, Y., and J. C. L. Chan, 2005: The East Asian summer monsoon: An overview. Meteorol. Atmos. Phys., 89, 117-142, https://doi.org/10.1007/s00703-005-0125-z.

——, X. Shi, Y. Liu, Y. Liu, Q. Li, Y. Qian, M. Miao, G. Zhai, and K. Gao, 2006a: Multi-year simulations and experimental seasonal predictions for rainy seasons in China by using a nested regional climate model (RegCM_NCC). Part I: Sensitivity study. Adv. Atmos. Sci., 23, 323-341, https://doi.org/10.1007/s00376-006-0323-8.

——, Y. Liu, X. Shi, Q. Li, Q. Li, and Y. Liu, 2006b: Multi-year simulations and experimental seasonal predictions for rainy seasons in China by using a nested regional climate model (RegCM_NCC) Part II: The experimental seasonal prediction. Adv. Atmos. Sci., 23, 487-503, https://doi.org/10.1007/s00376-006-0487-2.

Fennig, K., M. Schröder, and R. Hollmann, 2017: Fundamental Climate Data Record of Microwave Imager Radiances, Edition 3. https://doi.org/10.5676/EUM_SAF_CM/FCDR_MWI/V003.

Gandin, L. S and Murphy A. H., 1992: Equitable Skill Scores for Categorical Forecasts. Monthly Weather Review, 120, 361-370, https://doi.org/10.1175/1520-0493(1992)120<0361:ESSFCF>2.0.CO;2

Gelaro, R., and Coauthors, 2017: The Modern-Era Retrospective Analysis for Research and Applications, Version 2 (MERRA-2). J. Climate, 30, 5419–5454, https://doi.org/10.1175/JCLI-D-16-0758.1.

Giorgi, F., 2019: Thirty Years of Regional Climate Modeling: Where Are We and Where Are We Going next? J. Geophys. Res. Atmos., 124, 5696-5723, https://doi.org/10.1029/2018JD030094.

Griffies, S. M. and Coauthors, 2005: Formulation of an ocean model for global climate simulations. Ocean Science, 1, 45-79, https://doi.org/10.5194/os-1-45-2005.

Accepted for publication in *Journal of Climate*. DOI 10.1175/JCLI-D-23-0565.1.

Gu, H., Xu, YP., Liu, L. et al., 2023 Seasonal catchment memory of high mountain rivers in the Tibetan Plateau. Nat Commun 14, 3173. https://doi.org/10.1038/s41467-023-38966-9

Hall, D. K., and G. A. Riggs, 2021: MODIS/Terra Snow Cover Daily L3 Global 0.05Deg CMG, Version 61. https://doi.org/10.5067/MODIS/MOD10C1.061.

Harris, I., P. D. Jones, T. J. Osborn, and D. H. Lister, 2014: Updated high-resolution grids of monthly climatic observations - the CRU TS3.10 Dataset. Int. J. Climatol., 34, 623-642, https://doi.org/10.1002/joc.3711.

Hersbach, H., and Coauthors, 2020: The ERA5 global reanalysis. Quarterly Journal of the Royal Meteorological Society, 146, 1999–2049, https://doi.org/10.1002/qj.3803.

Holtslag, A. A. M., and B. A. Boville, 1993: Local Versus Nonlocal Boundary-Layer Diffusion in a Global Climate Model. J. Climate, 6, 1825-1842, https://doi.org/10.1175/1520-0442(1993)006<1825:LVNBLD>2.0.CO;2.

Hoskins, B. J., and D. J. Karoly, 1981: The Steady Linear Response of a Spherical Atmosphere to Thermal and Orographic Forcing. J. Atmos. Sci., 38, 1179-1196, https://doi.org/10.1175/1520-0469(1981)038<1179:TSLROA>2.0.CO;2.

Ji, J. J., M. Huang, and K. R. Li, 2008: Prediction of carbon exchanges between China terrestrial ecosystem and atmosphere in 21st century. Sci. China Ser. D-Earth Sci, 51, 885-898, https://doi.org/10.1007/s11430-008-0039-y.

Jiang, J., Zhou, T., Qian, Y. et al., 2023 Precipitation regime changes in High Mountain Asia driven by cleaner air. Nature 623, 544–549. https://doi.org/10.1038/s41586-023-06619-y

Jiang, R., L. Sun, C. Sun, and X.-Z. Liang, 2021: CWRF downscaling and understanding of China precipitation projections. Climate Dyn., 57, 1079-1096, https://doi.org/10.1007/s00382-021-05759-z.

Kahn, R. A., 2005: Multiangle Imaging Spectroradiometer (MISR) global aerosol optical depth validation based on 2 years of coincident Aerosol Robotic Network (AERONET) observations. J. Geophys. Res. Atmos., 110, D10S04, https://doi.org/10.1029/2004JD004706.

——, and Coauthors, 2007: Satellite-derived aerosol optical depth over dark water from MISR and MODIS: Comparisons with AERONET and implications for climatological studies. J. Geophys. Res. Atmos., 112, D18205, https://doi.org/10.1029/2006JD008175.

Accepted for publication in *Journal of Climate*. DOI 10.1175/JCLI-D-23-0565.1.

Kanamitsu, M., W. Ebisuzaki, J. Woollen, S.-K. Yang, J. J. Hnilo, M. Fiorino, and G. L. Potter, 2002: NCEP–DOE AMIP-II Reanalysis (R-2). Bull. Amer. Meteor. Soc., 83, 1631–1644, https://doi.org/10.1175/BAMS-83-11-1631.

Kistler, R. and Coauthors, 2001: The NCEP-NCAR 50-year reanalysis: Monthly means CD-ROM and documentation. Bull. Amer. Meteor. Soc., 82, 247-267, https://doi.org/10.1175/1520-0477(2001)082<0247:TNNYRM>2.3.CO;2.

Koster, R. D. and Coauthors, 2004: Realistic Initialization of Land Surface States: Impacts on Subseasonal Forecast Skill. J. Hydrometeor., 5, 1049-1063, https://doi.org/10.1175/JHM-387.1.

Lau, W. K. M., and S. Yang, 1996: Seasonal variation, abrupt transition, and intraseasonal variability associated with the asian summer monsoon in the GLA GCM. J. Climate, 9, 965-985, https://doi.org/10.1175/1520-0442(1996)009<0965:SVATAI>2.0.CO;2.

Li, C., H. Lu, K. Yang, J. S. Wright, L. Yu, Y. Chen, X. Huang, and S. Xu, 2017: Evaluation of the Common Land Model (CoLM) from the perspective of water and energy budget simulation: Towards inclusion in CMIP6. Atmosphere, 8, 141, https://doi.org/10.3390/atmos8080141.

Li, Q., T. Wang, F. Wang, X.-Z. Liang, C. Zhao, L. Dong, C. Zhao, and B. Xie, 2021: Dynamical downscaling simulation of the East Asian summer monsoon in a regional Climate-Weather Research and Forecasting model. Int. J. Climatol., 41, E1700-E1716, https://doi.org/10.1002/joc.6800.

Li, Z. chao, Z. gang Wei, C. Wang, Z. yuan Zheng, H. Wei, and H. Liu, 2012: Simulation and improvement of common land model on the bare soil of Loess Plateau underlying surface. Environ. Earth Sci., 66, 1091-1097, https://doi.org/10.1007/s12665-011-1315-2.

Liang, X.-Z., and W. C. Wang, 1998: Associations between China monsoon rainfall and tropospheric jets. Quart. J. Roy. Meteor. Soc., 124, 2597-2623, https://doi.org/10.1256/smsqj.55203.

——, A. N. Samel, and W. C. Wang, 1995: Observed and GCM simulated decadal variability of monsoon rainfall in east China. Climate Dyn., 11, 103-114, https://doi.org/10.1007/BF00211676.

Accepted for publication in *Journal of Climate*. DOI 10.1175/JCLI-D-23-0565.1.

——, K. E. Kunkel, and A. N. Samel, 2001: Development of a regional climate model for U.S. Midwest applications. Part I: Sensitivity to buffer zone treatment. J. Climate, 14, 4363-4378, https://doi.org/10.1175/1520-0442(2001)014<4363:DOARCM>2.0.CO;2.

——, L. Li, A. Dai, and K. E. Kunkel, 2004: Regional climate model simulation of summer precipitation diurnal cycle over the United States. Geophys. Res. Lett., 31, L24208, https://doi.org/10.1029/2004GL021054.

——, and Coauthors, 2005: Development of land surface albedo parameterization based on moderate resolution imaging spectroradiometer (MODIS) data. J. Geophys. Res. Atmos., 110, 1-22, https://doi.org/10.1029/2004JD005579.

——, J. Pan, J. Zhu, K. E. Kunkel, J. X. L. Wang, and A. Dai, 2006a: Regional climate model downscaling of the U.S. summer climate and future change. J. Geophys. Res. Atmos., 111, D10108, https://doi.org/10.1029/2005JD006685.

——, M. Xu, H. I. Choi, K. E. Kunkel, L. Rontu, J.-F. Geleyn, M. D. Müller, E. Joseph, and J. X. Wang, 2006b: Development of the regional climate-weather research and forecasting model (CWRF): Treatment of subgrid topography effects. Proceedings of the 7th annual WRF user's workshop, Boulder, CO, Citeseer, 19-22.

——, X. Yuan, T. Ling, H. I. Choi, F. Zhang, L. Chen, S. Liu, S. Su, F. Qiao, Y. He, J. X. L. Wang, K. E. Kunkel, W. Gao, E. Joseph, V. Morris, T. W. Yu, J. Dudhia, and J. Michalakes, 2012: Regional climate-weather research and forecasting model. Bull. Amer. Meteor. Soc., 93, 1363-1387, https://doi.org/10.1175/BAMS-D-11-00180.1.

——, C. Sun, X. Zheng, Y. Dai, M. Xu, H. I. Choi, T. Ling, F. Qiao, X. Kong, X. Bi, L. Song, and F. Wang, 2019: CWRF performance at downscaling China climate characteristics. Climate Dyn., 52, 2159-2184, https://doi.org/10.1007/s00382-018-4257-5.

——, and Coauthors, 2024: DAWN: Dashboard for Agricultural Water Use and Nutrient Management—A Predictive Decision Support System to Improve Crop Production in a Changing Climate. Bull. Amer. Meteor. Soc., 105, E432–E441, https://doi.org/10.1175/BAMS-D-22-0221.1.

Lim, Y.-K., D. W. Shin, S. Cocke, T. E. Larow, J. T. Schoof, J. J. O'Brien, and E. P. Chassignet, 2007: Dynamically and statistically downscaled seasonal simulations of

Accepted for publication in *Journal of Climate*. DOI 10.1175/JCLI-D-23-0565.1.

maximum surface air temperature over the southeastern United States. J. Geophys. Res. Atmos., 112, D24102, https://doi.org/10.1029/2007JD008764.

Liu, S., X.-Z. Liang, W. Gao, and H. Zhang, 2008: Application of climate-weather research and forecasting model (CWRF) in China: domain optimization. Chi. J. Atmos. Sci., 32, 457-468, https://doi.org/10.3878/j.issn.1006-9895.2008.03.04.

——, W. Gao, and X.-Z. Liang, 2013: A regional climate model downscaling projection of China future climate change. Climate Dyn., 41, 1871-1884, https://doi.org/10.1007/s00382-012-1632-5.

——, J. X. L. Wang, X.-Z. Liang, and V. Morris, 2016: A hybrid approach to improving the skills of seasonal climate outlook at the regional scale. Climate Dyn., 46, 483-494, https://doi.org/10.1007/s00382-015-2594-1.

Luo, Y., H. Wang, R. Zhang, W. Qian, and Z. Luo, 2013: Comparison of Rainfall Characteristics and Convective Properties of Monsoon Precipitation Systems over South China and the Yangtze and Huai River Basin. J. Climate., 26, 110-132, https://doi.org/10.1175/JCLI-D-12-00100.1.

Ma, J., H. Wang, and K. Fan, 2015: Dynamic Downscaling of Summer Precipitation Prediction over China in 1998 Using WRF and CCSM4. Adv. Atmos. Sci., 32, 577-584, https://doi.org/10.1007/s00376-014-4143-y.

Niu, G. Y. and Z. L. Yang, 2007: An observation-based formulation of snow cover fraction and its evaluation over large North American river basins. J. Geophys. Res. Atmos., 112, D21101, https://doi.org/10.1029/2007JD008674.

Notaro, M., 2008: Statistical identification of global hot spots in soil moisture feedbacks among IPCC AR4 models. J. Geophys. Res. Atmos., 113, D09101, https:// doi.org/10.1029/2007JD009199.

Orsolini, Y. J., R. Senan, G. Balsamo, F. J. Doblas-Reyes, F. Vitart, A. Weisheimer, A. Carrasco, and R. E. Benestad, 2013: Impact of snow initialization on sub-seasonal forecasts. Climate Dyn., 41, 1969-1982, https://doi.org/10.1007/s00382-013-1782-0.

Patarčić, M., and Č. Branković, 2012: Skill of 2-m Temperature Seasonal Forecasts over Europe in ECMWF and RegCM Models. Mon. Wea. Rev., 140, 1326-1346, https://doi.org/10.1175/MWR-D-11-00104.1.

Accepted for publication in *Journal of Climate*. DOI 10.1175/JCLI-D-23-0565.1.

Prein, A. F. and Coauthors, 2015: A review on regional convection-permitting climate modeling: Demonstrations, prospects, and challenges. Rev. Geophys., 53, 323-361, https://doi.org/10.1002/2014RG000475.

Prodhomme, C., F. J. Doblas-Reyes, O. Bellprat, and E. Dutra, 2016: Impact of land-surface initialization on sub-seasonal to seasonal forecasts over Europe. Climate Dyn., 47, 919-935, https://doi.org/10.1007/s00382-015-2879-4.

Qiao, F., and X. Z. Liang, 2015: Effects of cumulus parameterizations on predictions of summer flood in the Central United States. Climate Dyn., 45, 727-744, https://doi.org/10.1007/s00382-014-2301-7.

——, and X.-Z. Liang, 2016: Effects of cumulus parameterization closures on simulations of summer precipitation over the United States coastal oceans: U.S. Coastal Ocean Summer Rainfall Simulation and the Cumulus Closure Effects. J. Adv. Model. Earth Syst., 8, 764-785, https://doi.org/10.1002/2015MS000621.

——, and ——, 2017: Effects of cumulus parameterization closures on simulations of summer precipitation over the continental United States. Climate Dyn., 49, 225-247, https://doi.org/10.1007/s00382-016-3338-6.

Ren, H., and Coauthors, 2019: The China Multi-Model Ensemble Prediction System and Its Application to Flood-Season Prediction in 2018. J Meteorol Res 33, 540-552, https://doi.org/10.1007/s13351-019-8154-6.

Roads, J., S.-C. Chen, and M. Kanamitsu, 2003: U.S. regional climate simulations and seasonal forecasts. J. Geophys. Res. Atmos., 108, https://doi.org/10.1029/2002JD002232.

Rontu, L., 2006: A study on parametrization of orography-related momentum fluxes in a synoptic-scale NWP model. Tellus A: Dynamic Meteorology and Oceanography, 58, 69-81, https://doi.org/10.1111/j.1600-0870.2006.00162.x.

Rummukainen, M., 2016: Added value in regional climate modeling. Wiley Interdiscip. Rev.-Clim. Chang., 7, 145-159, https://doi.org/10.1002/wcc.378.

Samel, A. N., W. C. Wang, and X.-Z. Liang, 1999: The monsoon rainband over China and relationships with the Eurasian circulation. J. Climate, 12, 115-131, https://doi.org/10.1175/1520-0442-12.1.115.

Accepted for publication in *Journal of Climate*. DOI 10.1175/JCLI-D-23-0565.1.

Sangelantoni, L., R. Ferretti, and G. Redaelli, 2019: Toward a Regional-Scale Seasonal Climate Prediction System over Central Italy Based on Dynamical Downscaling. Climate, 7, 120, https://doi.org/10.3390/cli7100120.

Shi, W., H. Chen, and X.-Z. Liang, 2021: CWRF-based ensemble simulation of tropical cyclone activity near China and its sensitivity to the model physical parameterization schemes. Atmos. Oceanic Sci. Lett., 14, 100004, https://doi.org/10.1016/j.aosl.2020.100004.

Sun, C., and X.-Z. Liang, 2020a: Improving US extreme precipitation simulation: dependence on cumulus parameterization and underlying mechanism. Climate Dyn., 55, 1325-1352, https://doi.org/10.1007/s00382-020-05328-w.

——, and ——, 2020b: Improving US extreme precipitation simulation: sensitivity to physics parameterizations. Climate Dyn., 54, 4891-4918, https://doi.org/10.1007/s00382-020-05267-6.

——, and ——, 2022: Understanding and Reducing Warm and Dry Summer Biases in the Central United States: Improving Cumulus Parameterization. J. Climate, 1-43, https://doi.org/10.1175/JCLI-D-22-0254.1.

——, and ——, 2023: Understanding and Reducing Warm and Dry Summer Biases in the Central United States: Analytical Modeling to Identify the Mechanisms for CMIP Ensemble Error Spread. J. Climate, 36, 2035-2054, https://doi.org/10.1175/JCLI-D-22-0255.1.

Sun, L., H. Li, S. E. Zebiak, D. F. Moncunill, F. D. A. D. S. Filho, and A. D. Moura, 2006: An Operational Dynamical Downscaling Prediction System for Nordeste Brazil and the 2002-04 Real-Time Forecast Evaluation. J. Climate, 19, 1990-2007, https://doi.org/10.1175/JCLI3715.1.

Tao, W.-K., J. Simpson, D. Baker, S. Braun, M.-D. Chou, B. Ferrier, D. Johnson, A. Khain, S. Lang, and B. Lynn, 2003: Microphysics, radiation and surface processes in the Goddard Cumulus Ensemble (GCE) model. https://ntrs.nasa.gov/citations/20010037610.

Thomas, J. A., A. A. Berg, and W. J. Merryfield, 2016: Influence of snow and soil moisture initialization on sub-seasonal predictability and forecast skill in boreal spring. Climate Dyn., 47, 49-65, https://doi.org/10.1007/s00382-015-2821-9.

Accepted for publication in *Journal of Climate*. DOI 10.1175/JCLI-D-23-0565.1.

Van, T. P., H. V. Nguyen, L. T. Tuan, T. N. Quang, T. Ngo-Duc, P. Laux, and T. N. Xuan, 2014: Seasonal Prediction of Surface Air Temperature across Vietnam Using the Regional Climate Model Version 4.2 (RegCM4.2). Adv. Meteorol., 2014, 245104, https://doi.org/10.1155/2014/245104.

Viovy, N., 2018: CRUNCEP Version 7 - Atmospheric Forcing Data for the Community Land Model. Research Data Archive at the National Center for Atmospheric Research, Computational and Information Systems Laboratory, https://doi.org/10.5065/PZ8F-F017.

Wang, B., 1987: The Development Mechanism for Tibetan Plateau Warm Vortices. J. Atmos. Sci., 44, 2978-2994, https://doi.org/10.1175/1520-0469(1987)044<2978:TDMFTP>2.0.CO;2.

Wang, C., X.-Z. Liang, and A. N. Samel, 2011: AMIP GCM Simulations of Precipitation Variability over the Yangtze River Valley. J. Climate, 24, 2116-2133, https://doi.org/10.1175/2011JCLI3631.1.

——, K. Yang, Y. Li, D. Wu, and Y. Bo, 2017: Impacts of Spatiotemporal Anomalies of Tibetan Plateau Snow Cover on Summer Precipitation in Eastern China. J. Climate, 30, 885-903, https://doi.org/10.1175/JCLI-D-16-0041.1.

Wang, H., K. Fan, J. Sun, S. Li, Z. Lin, G. Zhou, L. Chen, X. Lang, F. Li, Y. Zhu, H. Chen, and F. Zheng, 2015: A review of seasonal climate prediction research in China. Adv. Atmos. Sci., 32, 149-168, https://doi.org/10.1007/s00376-014-0016-7.

——, Y. Dai, S. Yang, T. Li, J. Luo, B. Sun, M. Duan, J. Ma, Z. Yin, and Y. Huang, 2022: Predicting climate anomalies: A real challenge. Atmos. Oceanic Sci. Lett., 15, 100115, https://doi.org/10.1016/j.aosl.2021.100115.

Wang, Y.-P., and R. Leuning, 1998: A two-leaf model for canopy conductance, photosynthesis and partitioning of available energy I:: Model description and comparison with a multi-layered model. Agric. For. Meteor,, 91, 89–111, https://doi.org/10.1016/S0168-1923(98)00061-6.

Wang, Z., A. Duan and G. Wu, 2014: Time-lagged impact of spring sensible heat over the Tibetan Plateau on the summer rainfall anomaly in East China: Case studies using the WRF model. Climate Dyn., 42, 2885-2898, https://doi.org/10.1007/s00382-013-1800-2.

Accepted for publication in *Journal of Climate*. DOI 10.1175/JCLI-D-23-0565.1.

Wei, J., J. Zhao, H. Chen, and X.-Z. Liang, 2021: Coupling Between Land Surface Fluxes and Lifting Condensation Level: Mechanisms and Sensitivity to Model Physics Parameterizations. J. Geophys. Res. Atmos., 126, https://doi.org/10.1029/2020JD034313.

Winton, M., 2000: A Reformulated Three-Layer Sea Ice Model. J. Atmos. Oceanic Technol., 17, 525-531, https://doi.org/10.1175/1520-0426(2000)017<0525:ARTLSI>2.0.CO;2.

Wu, J., and X. Gao, 2013: A gridded daily observation dataset over China region and comparison with the other datasets. Acta Geophysica Sinica, 56, 1102-1111, https://doi.org/10.6038/cjg20130406.

Wu, T., and Coauthors, 2014: An overview of BCC climate system model development and application for climate change studies. J. Meteor. Res., 28, 34-56, https://doi.org/10.1007/s13351-014-3041-7.

Xin, Y., Y. Dai, J. Li, X. Rong, and G. Zhang, 2019: Coupling the Common Land Model to ECHAM5 Atmospheric General Circulation Model. J. Meteor. Res., 33, 251-263, https://doi.org/10.1007/s13351-019-8117-y.

Xu, H., X.-Z. Liang, and Y. Xue, 2022: Regional climate modeling to understand Tibetan heating remote impacts on East China precipitation. Climate Dyn., https://doi.org/10.1007/s00382-022-06266-5.

Xu, K.-M., and D. A. Randall, 1996: A Semiempirical Cloudiness Parameterization for Use in Climate Models. J. Atmos. Sci., 53, 3084-3102, https://doi.org/10.1175/1520-0469(1996)053<3084:ASCPFU>2.0.CO;2.

Xue, Y., Z. Janjic, J. Dudhia, R. Vasic, and F. De Sales, 2014: A review on regional dynamical downscaling in intraseasonal to seasonal simulation/prediction and major factors that affect downscaling ability. Atmos. Res., 147-148, 68-85, https://doi.org/10.1016/j.atmosres.2014.05.001.

——, and Coauthors, 2021: Impact of Initialized Land Surface Temperature and Snowpack on Subseasonal to Seasonal Prediction Project, Phase i (LS4P-I): Organization and experimental design. Geosci. Model Dev., 14, 4465-4494, https://doi.org/10.5194/gmd-14-4465-2021.

Accepted for publication in *Journal of Climate*. DOI 10.1175/JCLI-D-23-0565.1.

——, and Coauthors, 2022: Spring Land Temperature in Tibetan Plateau and Global-Scale Summer Precipitation: Initialization and Improved Prediction. Bull. Amer. Meteor. Soc., 103, E2756-E2767, https://doi.org/10.1175/BAMS-D-21-0270.1.

——, and Coauthors, 2023: Remote effects of Tibetan Plateau spring land temperature on global subseasonal to seasonal precipitation prediction and comparison with effects of sea surface temperature: the GEWEX/LS4P Phase I experiment. Climate Dyn., https://doi.org/10.1007/s00382-023-06905-5.

Yang, S., K.-M. Lau, S.-H. Yoo, J. L. Kinter, K. Miyakoda, and C.-H. Ho, 2004: Upstream Subtropical Signals Preceding the Asian Summer Monsoon Circulation. J. Climate, 17, 4213-4229, https://doi.org/10.1175/JCLI3192.1.

Yatagai, A., A. Kitoh, K. Kamiguchi, O. Arakawa, H. Kawamoto, T. Watanabe, J. Kubota, M. Taniguchi, and S. Kanae, 2007: Asian Precipitation : Highly Resolved Observational Data Integration Towards Evaluation of the Water Resources. https://www2.jpgu.org/meeting/2010_disc1/program/PDF/A-AS004/AAS004-04.pdf

Yuan, X., and X.-Z. Liang, 2011a: Improving cold season precipitation prediction by the nested CWRF-CFS system. Geophys. Res. Lett., 38, L02706, https://doi.org/10.1029/2010GL046104.

——, and ——, 2011b: Evaluation of a Conjunctive Surface-Subsurface Process Model (CSSP) over the Contiguous United States at Regional-Local Scales. J. Hydrometeor., 12, 579-599, https://doi.org/10.1175/2010JHM1302.1.

——, ——, and E. F. Wood, 2012: WRF ensemble downscaling seasonal forecasts of China winter precipitation during 1982-2008. Climate Dyn., 39, 2041-2058, https://doi.org/10.1007/s00382-011-1241-8.

Zhang, F., X.-Z. Liang, J. Li, and Q. Zeng, 2013a: Dominant roles of subgrid-scale cloud structures in model diversity of cloud radiative effects: SUBGRID CLOUD STRUCTURE IN MODEL SPREAD. J. Geophys. Res. Atmos., 118, 7733-7749, https://doi.org/10.1002/jgrd.50604.

——, ——, Q. Zeng, Y. Gu, and S. Su, 2013b: Cloud-Aerosol-Radiation (CAR) ensemble modeling system: Overall accuracy and efficiency. Adv. Atmos. Sci., 30, 955-973, https://doi.org/10.1007/s00376-012-2171-z.

Accepted for publication in *Journal of Climate*. DOI 10.1175/JCLI-D-23-0565.1.

Zhang H., X.-Z. Liang, F. Wang, B. Xie, Q. Q. Li, 2023: Improving summer precipitation seasonal prediction in China using CWRF downscaling of BCC_CSM1.1m. Trans Atmos Sci,46(2),161-179, https://doi.org/10.13878/j.cnki.dqkxxb.20210116001

Zhang, S., M. Wang, L. Wang, X.-Z. Liang, C. Sun, and Q. Li, 2023: Sensitivity of the simulation of extreme precipitation events in China to different cumulus parameterization schemes and the underlying mechanisms. Atmos. Res., 285, 106636, https://doi.org/10.1016/j.atmosres.2023.106636.

Zhao, G., L. Di Girolamo, S. Dey, A. L. Jones, and M. Bull, 2009: Examination of direct cumulus contamination on MISR-retrieved aerosol optical depth and angstrom coefficient over ocean. Geophys. Res. Lett., 36, L13811, https://doi.org/10.1029/2009GL038549.

Zhao, Y., and X.-Z. Liang, 2023: Enhancing summer extreme precipitation prediction in the Yangtze River Basin through CWRF downscaling and its skillful multi-physics ensemble approach. Climate Dyn., https://doi.org/10.1007/s00382-024-07153-x.

Zhao, Y., F. Qiao, X.-Z. Liang, and J. Yu, 2023: Understanding and improving Yangtze River Basin summer precipitation prediction using an optimal multi-physics ensemble. Front. Earth Sci., https://doi.org/10.1007/s11707-024-1118-x.

Zuo, Z., S. Yang, W. Wang, A. Kumar, Y. Xue, and R. Zhang, 2011: Relationship between anomalies of Eurasian snow and southern China rainfall in winter. Environ. Res. Lett., 6, 045402, https://doi.org/10.1088/1748-9326/6/4/045402.

Accepted for publication in *Journal of Climate*. DOI 10.1175/JCLI-D-23-0565.1.